THE ASTROPHYSICAL JOURNAL SUPPLEMENT SERIES, 55:533–550, 1984 July

WIDE-ANGLE RADIO TAIL QSOs AS MEMBERS OF CLUSTERS OF GALAXIES. II. DIRECT OPTICAL OBSERVATIONS AND SPECTROSCOPY OF QSO FIELDS

PAUL HINTZEN[1]
Laboratory for Astronomy and Solar Physics, NASA/Goddard Space Flight Center
Received 1983 July 17; accepted 1983 December 28

ABSTRACT

Deep direct observations ($R \approx 23$) have been obtained for the fields of 19 radio QSOs with $0.3 < z < 1.5$, including both wide-angle radio tail QSOs and undistorted "comparison" QSOs. After correction for background galaxies, the fields observed contain from 0 to 22 excess galaxies within $\sim 35''$ of each QSO. The number of excess galaxies detected drops precipitously for $z > 0.65$. A comparison of excess galaxy counts in the low redshift QSO fields with those in the high redshift QSO fields supports the cosmological interpretation of QSO redshifts at the 99% significance level. Our direct data therefore provide independent confirmation of the results of Stockton's spectroscopic study. Among the low-redshift QSOs, the radio-tail QSO fields contain, on average, 3 times as many excess galaxies as do the fields of the undistorted comparison QSOs. This result has a statistical significance of 97%, and we conclude that wide-angle radio tail QSOs are generally associated with richer concentrations of galaxies than are undistorted QSOs. This implies that distortions of QSO radio structures are produced by interaction with an intracluster medium, or by interaction of the radio lobes with nearby galaxies.

Resolved components have been detected underlying the stellar nuclei of several of the QSOs observed. The objects resolved include 3C275.1 and 3C334, both of which have $z = 0.555$, making them the highest redshift QSOs which have been resolved to date. The elliptical nebulosity underlying 3C275.1 has a $14''$ major axis, implying a much larger physical size than has previously been reported for the resolved components of QSOs.

Spectroscopy with the cryogenic camera on the KPNO 4 m telescope has provided redshifts for eight galaxies in three of the QSO fields containing excess galaxies: 0003+158, 0214+108, and 3C275.1. Four of these eight galaxies, including at least one in each field, have velocities with respect to the corresponding QSOs of less than 600 km s^{-1}. Since the probability of these redshift coincidences occurring by chance is less than 10^{-3}, this result indicates that the excess galaxies discussed above do indeed have the same redshifts as the QSOs they appear to lie near.

Four of the galaxies for which redshifts were obtained are in the 3C275.1 field, which contains 22 excess galaxies within $35''$ of the QSO. The two brighter galaxies observed are foreground objects, as expected. The two fainter galaxies have essentially the same redshift as the QSO ($z = 0.555$), supporting the suggestion of Hintzen, Boeshaar, and Scott that 3C275.1 lies at the center of a rich cluster of galaxies, the first such instance identified. The size of the nebulosity underlying 3C275.1, noted earlier, implies that this QSO may lie in the first-ranked cluster galaxy, which could be a cD.

Our results indicate that deep CCD observations of wide-angle radio tail QSOs would provide a sample of distant clusters of galaxies at extremely large, but well-determined redshifts. Such a sample could then be used to study the evolution of clusters and their constituent galaxies and might allow an accurate determination of q_0. Observing RT QSOs rather than a general sample of high redshift QSOs should ensure the presence of a QSO-associated cluster in each field, minimizing the formidable problem of contamination by foreground and background clusters.

Subject headings: galaxies: clustering — galaxies: redshifts — quasars

I. INTRODUCTION

The identification of a significant sample of clusters of galaxies associated with QSOs would have great impact on our understanding of the QSO phenomenon, the evolution of galaxies and clusters of galaxies, and basic cosmological parameters. We have suggested that wide-angle radio tail QSOs (RT QSOs) are members of clusters of galaxies containing dense intracluster media (Hintzen, Boeshaar, and Sco 1981; Hintzen, Ulvestad, and Owen 1983; hereafter HBS an HUO, respectively). If so, deep CCD observations of the fiel of such QSOs would provide a sample of clusters of galaxies known, very large redshifts ($z > 1$). Such a sample could th be used to study the evolution of clusters and their constitue galaxies and might allow an accurate determination of q_0 v the angular size–redshift relation (e.g., Bruzual and Spinr 1978). Observing RT QSOs rather than a random sample high redshift QSOs would ensure to first order that the clust detected were actually QSO-associated, reducing contami

[1]Visiting Astronomer, Kitt Peak National Observatory, which is oper-d by Associated Universities for Research in Astronomy, Inc., under tract with the National Science Foundation.

tion by foreground and background clusters, a major problem at large redshifts. In order to test the hypothesis that RT QSOs are members of clusters of galaxies, we have obtained deep direct video camera observations ($R \approx 23$) of the fields of 19 QSOs ($0.3 < z < 1.5$), including both RT QSOs and undistorted "comparison" QSOs.

Even though observations designed to establish physical relationships between individual QSOs and clusters of galaxies have been pursued for close to two decades, such observations have met with comparatively little success, since only a handful of associations between QSOs and comparatively poor clusters of galaxies have been identified (Phillips 1980, and references therein; Wyckoff *et al.* 1980; Spinrad 1980; French and Gunn 1983). Furthermore, Roberts, O'Dell, and Burbidge (1977) demonstrated that there is no positional correlation between low redshift QSOs and Abell clusters, and they therefore argued that QSOs do not occur in the central regions of rich clusters of galaxies.

Oemler, Gunn, and Oke (1972) reported that the QSO 3C323.1 appears to be an outlying member of a rich Zwicky cluster, based on the concordant redshifts of the QSO and the cluster's cD galaxy. Recently, Margon, Downes, and Spinrad (1983) reported on similar spectroscopic grounds that the radio-quiet QSO 0015+162 is an outlying member of the rich, distant cluster 0016+16 (see Koo 1981). In both of these cases, however, the QSO lies at a projected distance of ~ 2 Mpc ($H_0 = 50$ km s^{-1} Mpc^{-1}) from the cluster center and could not have spent a significant portion of its lifetime in the dense environment of the cluster core. Even assuming that each QSO's true (unprojected) distance from the corresponding cluster center is only 2 Mpc and that each has been traveling radially away from the cluster center at a mean speed of 1000 km s^{-1}, it has been at least 10^9 yrs since either QSO was within 1 Mpc of the cluster center. Consequently, the physical conditions experienced by these two QSOs may not differ appreciably from the environment of those QSOs known to be in small groups or poor clusters of galaxies.

While Stockton (1978) showed that many QSOs are associated with single galaxies or small groups (two or three galaxies) at the QSOs' redshifts, he found no clusters associated with QSOs and has concluded that QSOs seldom, if ever, occur in the centers of rich clusters of galaxies (Stockton 1980). Indeed, the postulate that QSOs cannot exist in the dense environment at the center of rich clusters of galaxies is essential to some current models of the QSO phenomenon and quasar evolution (e.g., Stocke and Perrenod 1981).

Testing that postulate and identifying QSOs associated with clusters in general would be greatly facilitated if QSOs likely to be members of clusters could be identified in advance. Studies of radio galaxies with "tail-like" distortions in their radio maps indicate that substantial distortions occur only when the radio galaxy is a member of a cluster. While classical "head-tail" radio morphologies are found among cluster galaxies having low radio luminosities, many stronger sources associated with galaxies in clusters have proven to be "wide-angle radio tails" (Owen and Rudnick 1976). We have therefore suggested that in the search for substantial clusters of galaxies associated with QSOs, the most promising objects for study are those QSOs showing tail-like distortions in their radio morphologies (HBS).

Consequently, we obtained deep direct observations of two wide-angle radio tail QSOs, 3C275.1 ($z = 0.557$) and 3C270.1 ($z = 1.519$). These direct observations suggested that the quasar 3C275.1 lies in a first-ranked galaxy in the center of a rich, dense cluster of galaxies (HBS). We detected no sign of a cluster associated with the high redshift QSO 3C270.1, a result in keeping with the hypothesis that QSO redshifts are cosmological. Subsequently, Hintzen and Owen (1981) demonstrated that the BL Lac object 1400+162 is a wide-angle radio tail source. Baldwin *et al.* (1977) had already reported that 1400+162 appeared to be a member of a group of galaxies ($z = 0.245$), at least one of which has the same redshift as the BL Lac. Unpublished deep direct photography of 1400+162 suggests that this object may lie in a rich cluster (J. Hutchings, private communication). Recently, Harris *et al.* (1983) reported that the wide-angle radio tail QSO 4C 08.66N appears to lie in a cluster of galaxies, although spectroscopic confirmation of the association has not yet been obtained.

In view of these encouraging preliminary results, we undertook a VLA snapshot mapping survey of 117 radio quasars in order to identify wide-angle radio tail sources (HUO [Paper I]). Based on the fraction of sources which proved to be distorted, HUO concluded that at least 5%–17% of radio-loud QSOs are members of clusters of galaxies which are sufficiently rich to contain substantial intracluster media. In the present paper we discuss direct optical observations of a sample of QSOs selected from the radio observations reported in Paper I. Both wide-angle radio tail QSOs and undistorted "comparison" QSOs have been included in the optical observations. The first results from a spectroscopic study of galaxies detected in these fields are also reported, and these data provide preliminary confirmation that the QSO 3C275.1 lies at the center of a rich cluster.

II. THE QUASAR SAMPLE OBSERVED

In order to determine whether "bent" radio QSOs are members of clusters of galaxies, deep direct observations ($R \approx 23$) were obtained for 19 radio quasars with $0.3 < z < 1.5$, including both wide-angle radio tail objects (RT QSOs) and undistorted "comparison" QSOs. These observations, taken using R passbands with the video camera on the KPNO 4 m telescope, are sufficiently deep that clusters of galaxies with $z < 0.65$ should be detectable, although this limit will vary with evolutionary effects, cluster richness, and seeing.

The quasars for which direct optical data were obtained are listed in Table 1, which includes each object's radio source designation, redshift, and radio axis bending angle (Θ), as well as a summary of the galaxy counts in the appropriate video camera field. The radio data involved are discussed by HUO. Note that we have observed less than half of the sources with $\Theta > 20°$ listed by HUO, and, in addition, those objects observed do not include all of the best examples of wide-angle RT QSOs.

As noted by HUO, the radio axis bending angles for QSOs form a fairly continuous distribution spanning the range from $\Theta = 0°$ to $\Theta > 60°$, although the great majority of sources have suffered relatively little distortion. This continuous distribution suggests a continuum of quasar environments, with some QSOs lying in isolated galaxies, some in poor groups of galaxies, and some in comparatively rich clusters of galaxies

TABLE 1

QSO FIELDS OBSERVED

Radio	Object	z	Type	Θ	R(1st)	R(comp)	ΔM	$N_{22.5}$	$N_{\rm lim}$	$N_{\rm bg}$	$\Delta N_{\rm lim}$	$\Delta N_{\rm lim/A}$
4C15.01	0003+158	0.450	comp	0°	18.8	22.0	3.1	...	5	2.5	2.5	+10
3C37.....	0115+027	0.672	comp	8°	20.5	22.5	2.0	3	3	4.0	−1.0	−5
3C39.....	0118+034	0.765	comp	9°	21.1	22.5	1.4	7	7	4.0	3.0	+5
4C24.02	0130+242	0.457	comp	8°	18.8	22.5	3.6	6	6	4.0	2.0	+10
4C10.06	0214+108	0.408	comp	11°	18.6	22.0	3.4	...	5	2.5	2.5	+10
3CR 93	0340+048[a]	0.357	comp	...	18.0	21.0	3.0	...	1	1.0	0	0
3CR 215	0903+169[b]	0.411	dist	...	18.8	22.5	3.6	10	10	3.5	6.5	+30
4C00.34	0957+003	0.907	dist	21°	21.9	23.0	1.0	4	6	5.5	0.5	0
OL 564	1038+52A	0.677	dist	27°	20.7	22.0	1.3	...	3	2.5	0.5	0
3CR 249.1	1100+772	0.311	comp	9°	17.7	22.0	4.2	...	4	2.5	1.5	+10
3CR 270.1	1218+339	1.519	dist	43°	24.6	23.0	−1.6	5	7	6.0	1.0	0
4C21.35	1222+216	0.435	dist	64°	18.8	22.5	4.2	14	14	4.0	10.	+40
3CR 275.1	1241+166	0.557	dist	24°	19.8	23.0	3.2	19	28	6.0	22.	+70
4C−06.35.....	1335−061	0.625	dist	62°	20.2	23.0	2.8	10	14	6.0	8	+25
4C24.31	1423+242	0.649	dist	24°	20.4	23.5	3.1	8	12	9.0	3	+10
4C37.43	1512+370	0.371	comp	0°	18.3	22.5	4.2	12	12	4.0	8	+40
3CR 334.....	1618+177	0.555	comp	3°	19.7	23.0	3.8	7	11	5.5	5.5	+20
4C27.28	1741+279	0.372	dist	26°	18.3	23.0	4.5	9	11	5.5	5.5	+30
4C28.59	2353+283	0.731	dist?	28°	20.8	23.0	2.1	7	8	5.5	2.5	+5

NOTES

Col. (1)—Survey designation of the radio source associated with the QSO. Only one designation is given for each object. A 3C name is preferred, followed by a 4C designation. References to the radio surveys and the optical identifications can be found in Hewitt and Burbidge 1980 (HB).

Col. (2).—Coordinate designation of the QSO.

Col. (3).—QSO redshifts, taken from HB. The values for 1038+52A and 1423+242 are each based on a single line identified with Mg II λ2798 and are therefore somewhat uncertain.

Col. (4).—Each QSO is classified as "distorted" or "comparison" based on its bending angle (Θ).

Col. (5).—Radio axis bending angle for each radio source (HUO). Sources with $\Theta > 20°$ are considered distorted.

Col. (6).—Expected R magnitude of a first-rank cluster galaxy at the QSO's redshift, taken from Coleman, Wu, and Weedman 1980.

Col. (7).— R magnitude considered the field's *completeness* limit, i.e., the magnitude to which identifications should be complete. This completeness limit is generally ~ 0.5 mag brighter than the "detection" limit.

Col. (8).— R(comp)− R(1st).

Col. (9).—Number of galaxies with $R \leq 22.5$ inside the 1.17 square arcminute rectangle analyzed by FOCAS. Values are listed only for fields with completeness limits $R \geq 22.5$.

Col. (10).—Number of galaxies brighter than R(comp) inside the 1.17 square arcminute rectangle analyzed by FOCAS. The quantity $N_{\rm lim}$ will generally be smaller than the number of galaxies listed in Table 1 since some galaxies listed are fainter than R(comp) or outside the region analyzed by FOCAS.

Col. (11).—Number of background galaxies brighter than R(comp) expected within the region analyzed by FOCAS. The background galaxy density vs. R relation derived by Butcher and Oemler 1978 was corrected by 25%, as suggested by Butcher, Oemler, and Wells 1983, and then used to calculate $N_{\rm bg}$ after correcting R(comp) for galactic absorption in excess of the value at $b^{\rm II} = 90°$. The absorption correction applied was $A_R = 0.135\ (\csc|b| - 1)$, where the relation derived by Heiles 1976, eq. (8), was converted to the R filter using eq. (5) of Sandage 1973. The second term was added to normalize the extinction to $A_R = 0$ at $b^{\rm II} = 90°$, since Butcher and Oemler assumed extinction was absent at the poles.

Col. (12).—Number of excess galaxies within the FOCAS-reduced field brighter than R(comp), $\Delta N = N_{\rm lim} - N_{\rm bg}$.

Col. (13).—Number density of excess galaxies at the QSO's distance. Only galaxies brighter than the field completeness limit and lying within each 1.17 square arcminute FOCAS-reduced field are included. Values are in galaxies Mpc^{-2} and are rounded to multiples of 5. We assume $H_0 = 50$ km s^{-1} Mpc^{-1} and $q_0 = 0$.

[a] 0340+048 is classified as a double radio source (HUO), so no bending angle (Θ) is listed, but the optical QSO lies on the radio axis. We therefore classify 0340+048 as an undistorted comparison QSO.

[b] 0903+169 is an extremely complex source, so defining a meaningful bending angle is difficult, but we consider the source distorted (HUO).

containing dense intergalactic media (IGM). Note that the one-dimensional Θ classification system does not completely characterize the distortions observed (see HUO), and, of course, the Θ value chosen as a dividing line between "distorted" and "undistorted" sources is somewhat arbitrary. Also, the dense IGMs in rich clusters need not always produce distortions in extended radio sources, although it appears that in most cases (66%) they do (see Rudnick and Owen 1977). Even in poor Zwicky clusters a substantial portion of the radio sources (at least 40%) are head-tail or wide-angle tail sources (Burns and Gregory 1982). We therefore expect that the distorted QSOs will lie in significant clusters of galaxies, while most of the undistorted QSOs will not, although they may be members of poor groups of the type observed by Stockton.

Each quasar in Table 1 is designated "distorted" (radio axis bending angle exceeds 20°), "undistorted" ($\Theta < 15°$), or "possibly" distorted. The last category includes only 2353+283.

This source has a formal bending angle of 28°, but, based on the shape of its northern lobe, we suspect that higher resolution might reveal a straight-axis source similar to 1618+177 (HUO). Even among the nine other sources listed as distorted, the degree of distortion, the type of distortion, and quality of available radio maps varies considerably (see HUO). For instance, the VLA data published by HUO demonstrate that both 1222+216 and 1423+242 are bent triple sources ($\Theta = 64°$ and 24°, respectively), but further radio data are required to determine details of the source structures. Finally, the 20 cm map of 0903+169 (3C215; see HUO) is very complex, with at least five distinct flux peaks, one of which is coincident with the optical QSO. We have classified this source as distorted because its fragmented morphology suggests interaction with an outside medium, and, besides, any choice of "major components" results in a large value for Θ.

III. DIRECT OBSERVATIONS

a) *Photometry*

Deep direct observations for each of the fields listed were obtained using the video camera (ISIT) on the KPNO 4 m telescope. Detailed descriptions of the instrument and reduction facilities may be found in Butcher and Oemler (1978) and references therein. Integration times ranged from 13.6 to 120 minutes, depending on the QSO's redshift and time constraints. Fields in M92 and NGC 2419 containing faint photometric standards were also observed (Christian 1980).

The video camera at the 4 m Cassegrain focus produces pictures which are 256 pixels square at a scale of 0".292 per pixel. After corrections for field distortions in the ISIT, the effective field is ~ 65" square. Our observations were obtained with red passbands in order to enhance detection of any nebulosities underlying the QSOs. During the first observing run, a KPNO R filter was used (KP 1097), consisting of 2 mm of OG 570 and 3 mm of KG 3, which produce an effective wavelength of 6425 Å with a full width at half-maximum transmission (FWHM) of 1500 Å. For subsequent runs we used just the 2 mm of OG 570, which, coupled with the video camera's extended S20 response, provided an "R prime" passband which was somewhat broader (effective wavelength of ~ 6700 Å; FWHM ≈ 2000 Å).

The data frames were corrected for small-scale response variations and geometric distortion using standard software on the KPNO Cyber. Each QSO field was then analyzed using the FOCAS automated object detection and classification systems. The FOCAS software was developed at Bell Laboratories by J. Jarvis and A. Tyson, then rewritten and implemented on a KPNO VAX by F. Valdes (for details, see Valdes 1982). FOCAS was run with the detection and classification parameters set at their default values. The results agree well with independent visual identification and classification of objects, except in a few instances where FOCAS failed to separate close pairs of objects. Since FOCAS requires rectangular input fields, the curved borders of the video camera fields were trimmed slightly before FOCAS processing, so a few objects at the field edges were not detected by FOCAS and have not been included on our statistical analysis (§ V and Table 1).

The KPNO "Mountain Photometry" code (Mould *et al.* 1980) was used to determine instrumental R or R' magnitudes in apertures of seven pixels radius (4".2 diameter) for all objects in the fields observed. The R magnitudes (Christian 1980) of standard stars in the M92 and NGC 2419 fields were used to derive R and R' zero-point corrections for each frame of these fields.

The photometric zero-point corrections for each filter were then plotted as a function of seeing (standard star FWHM). Using these plots and the measured FWHM of the QSO and any bright stars in the field, the photometric zero-point correction for each field was determined by interpolation and corrected for extinction using a coefficient of 0.083 mag per air mass (Hayes 1982).

Even though the OG 570 does not provide a "standard" R passband, the zero-point corrections derived from the various standard stars observed in each field vary by at most 0.03 mag, so the photometric zero point in the OG 570 system (R' system) is well defined. Comparisons of data taken for the same fields on different nights indicate that the total errors in the zero-point corrections applied are ~ 0.1 mag.

The resulting photometry and FOCAS classifications (s = star, g = galaxy) are listed in Table 2. Photometry histograms for the galaxies in each field are provided in Figure 3. Objects classified as "E" (edge) are outside the FOCAS-reduced fields and are included in neither the histograms nor the statistical discussion in § V. Statistical errors derived from photon counts in the object and sky "apertures" are smaller than 0.04 mag for $R < R(\text{comp}) - 2$, rising to ~ 0.08 mag at $R = R(\text{comp}) - 1$ and 0.15 mag at $R = R(\text{comp})$. Magnitudes followed by question marks indicate objects for which photometry is uncertain due to their proximity to other objects or to the edge of the frame. Since finite apertures were used in generating the photometry in Table 2, the magnitudes listed for the galaxies are *not* "total" magnitudes (see Butcher, Oemler, and Wells 1983).

b) *Positional Data and Finding Charts*

Accurate optical positions *relative to the QSOs* were also derived for each of the objects detected. The video camera scale and zero-point positions for each field were determined from measurements of object positions on the POSS sky survey plates. The POSS coordinates for the brighter objects in the video camera fields were used in conjunction with the "Mountain Photometry" object coordinates to determine the video camera scale and orientation for each of the three observing runs. Coordinates for the objects in each field were then derived using the mean scale for the observing run involved. The POSS coordinates for the QSO at the center of each field were used to set the R.A. and decl. zero points.

The video camera scale, 0".292 ± 0".004 per pixel, remained constant within ~ 1.5% over 12 months of observations. The camera orientation with respect to the sky varied by only one-third of a degree. Since the coordinates for objects in each field are determined with respect to the QSO at the frame center, positional errors due to the uncertainties in the field scale and rotation will increase with distance from the frame center. Therefore, the *maximum* positional errors expected

TABLE 2

PHOTOMETRY AND FOCAS CLASSIFICATIONS

Object	α(1950)	δ(1950)	R'_7	Class
		0003+158		
01[a]	00h03m25s09	+15°53′05″.9	15.4	s
02	00 03 27.05	+15 53 22.3	16.4	s
03	00 03 26.22	+15 53 11.9	20.8	g
04	00 03 25.70	+15 53 25.1	21.4	g
05	00 03 24.01	+15 52 58.1	20.5	g
06	00 03 24.28	+15 52 52.9	21.5	g
07	00 03 25.07	+15 52 39.8	21.6	g
08	00 03 26.28	+15 53 01.9	23.	g
09	00 03 24.13	+15 53 17.7	23.	s
11	00 03 23.62	+15 52 45.9	21.3	s
		0115+027		
01[a]	01h15m43s64	+02°42′19″.7	17.0	s
02	01 15 44.36	+02 42 02.6	19.9	s
03	01 15 42.70	+02 41 55.2	18.5	s
04	01 15 45.63	+02 42 06.5	19.8	g
05	01 15 45.91	+02 42 08.3	19.5?	g, E
06	01 15 43.82	+02 41 51.0	22.1	g
08	01 15 43.04	+02 42 05.7	22.5	s
10	01 15 43.29	+02 42 48.5	22.2	g
11	01 15 44.22	+02 42 51.2	22.2	E
		0118+034		
01[a]	01h18m26s12	+03°28′29″.9	17.9	s
02	01 18 26.14	+03 28 50.7	17.3	s
03	01 18 24.91	+03 28 22.2	20.7	g
04	01 18 25.02	+03 28 17.1	21.4	g
05	01 18 25.61	+03 28 19.0	21.4	g
06	01 18 27.15	+03 28 19.3	21.5	g
07	01 18 24.89	+03 28 02.5	21.5	g
09	01 18 27.84	+03 28 56.1	21.3	g
11	01 18 25.80	+03 28 59.7	22.3	s
12	01 18 24.63	+03 29 00.1	22.3	g
13	01 18 25.86	+03 28 24.0	22.9?	g?
		0130+242		
01[a]	01h30m39s08	+24°12′18″.8	17.3	s
02	01 30 40.56	+24 12 42.1	22.2	g?
03	01 30 39.70	+24 12 30.8	21.8	g
04	01 30 39.60	+24 12 22.1	21.8	g
05	01 30 39.44	+24 12 07.7	21.3	g
06	01 30 37.56	+24 12 49.6	21.9	g
07	01 30 36.98	+24 12 22.1	22.3	g
		0214+108		
01[a]	02h14m26s70	+10°50′17″.9	15.8	s
02	02 14 27.19	+10 50 06.7	17.5	s
03	02 14 26.32	+10 49 45.5	20.2	g
04	02 14 28.42	+10 50 11.1	20.4	g
05	02 14 27.84	+10 50 19.6	21.7	g
06	02 14 27.18	+10 50 31.5	22.4	g
07	02 14 25.48	+10 50 24.3	21.4	s
08	02 14 25.44	+10 50 18.1	22.0	g
10	02 14 25.96	+10 50 03.2	21.8?	g
		0340+048		
01[a]	03h40m51s57	+04°48′20″.6	18.2	s
02	03 40 52.19	+04 48 33.8	21.1	s
03	03 40 52.88	+04 48 26.4	21.0	g

Object	α(1950)	δ(1950)	R'_7	Class
		0903+169		
01[b]	09h03m44s15	+16°58′15″.9	18.5	g
02	09 03 44.82	+16 58 09.7	16.9	s
04	09 03 44.60	+16 58 03.8	20.0	g
05	09 03 44.19	+16 58 04.7	21.0	s
06	09 03 43.91	+16 57 52.1	19.9	g
07	09 03 43.63	+16 57 59.7	21.9	g
08	09 03 44.41	+16 57 59.0	21.9	g
11	09 03 45.04	+16 58 15.7	22.0	g
12	09 03 45.54	+16 58 27.6	21.8	g
13	09 03 44.43	+16 58 34.0	22.3	g
15	09 03 42.78	+16 58 33.3	22.1	g
16	09 03 42.70	+16 58 18.9	22.0	s
17	09 03 42.35	+16 58 10.1	19.7	g
21	09 03 45.94	+16 58 46.7	22.7?	g
24	09 03 45.12	+16 58 03.5	23.2	s
25	09 03 44.49	+16 58 08.9	21.9	g
		0957+003		
01[a]	09h57m43s75	+00°19′49″.2	17.4	s
02	09 57 44.32	+00 19 52.8	17.0	s
03	09 57 45.76	+00 20 11.8	18.8	s
04	09 57 45.10	+00 19 26.4	20.8	g
05	09 57 44.80	+00 19 24.2	21.5	g
07	09 57 44.61	+00 19 30.2	22.8	g
08	09 57 42.95	+00 19 42.0	22.3	g
09	09 57 42.89	+00 19 45.2	22.4	g
10	09 57 42.45	+00 19 41.6	23.5	g
11	09 57 44.66	+00 19 52.9	22.2?	g
13	09 57 43.23	+00 19 57.9	23.5	s
15	09 57 44.30	+00 20 04.3	23.1	g
16	09 57 42.78	+00 19 30.9	23.2	g
17	09 57 43.66	+00 20 07.2	23.1	g
		1038+52		
01[a]	10h38m43s08	+52°49′10″.3	16.6	s
02	10 38 43.35	+52 49 17.8	20.9	g
03	10 38 44.14	+52 49 19.8	21.3	s
04	10 38 44.10	+52 49 40.7	18.4	s, E
05	10 38 45.14	+52 49 37.9	18.3	g?, E
06	10 38 45.34	+52 49 07.4	22.2	g
07	10 38 45.60	+52 49 07.1	21.8	g
08	10 38 46.49	+52 49 02.3	19.7	g
09	10 38 42.45	+52 49 00.3	21.5	s
		1100+772		
01[a]	11h00m27s61	+77°15′08″.3	15.9	s
02	11 00 21.19	+77 14 53.1	21.3	g
03	11 00 33.96	+77 15 22.1	18.5	s
04	11 00 35.93	+77 15 04.7	21.9	g
05	11 00 30.38	+77 15 21.9	21.9	g
06	11 00 35.03	+77 14 35.6	21.6	g
07	11 00 36.58	+77 15 15.6	22.5	g?
		1222+216		
01[a]	12h22m23s44	+21°39′23″.5	16.8	s
02	12 22 23.98	+21 39 17.8	20.7	g
03	12 22 24.71	+21 39 15.1	20.9	g
04	12 22 23.92	+21 39 00.3	19.7	g
05	12 22 23.50	+21 38 55.3	20.0	g
06	12 22 22.57	+21 39 06.4	20.4	g

TABLE 2—*Continued*

Object	α(1950)	δ(1950)	R'_7	Class
07	12 22 22.48	+21 39 28.5	21.8	g
08	12 22 22.01	+21 39 20.8	22.6	s
09	12 22 21.60	+21 39 21.2	21.6	g
10	12 22 21.54	+21 39 33.3	19.7	g
11	12 22 23.96	+21 39 31.8	23.3	g
12	12 22 24.09	+21 39 44.0	22.2	g
13	12 22 24.96	+21 39 40.1	20.8	g
14	12 22 25.67	+21 39 49.4	19.?	g
15	12 22 25.47	+21 39 26.6	23.3	s
16	12 22 23.07	+21 39 32.5	22.7	s
17	12 22 21.98	+21 39 09.5	22.5	g
18	12 22 24.80	+21 39 13.2	21.7	g
19	12 22 24.79	+21 39 32.7	22.4	g
20	12 22 23.92	+21 39 36.1	22.6?	?
21	12 22 23.69	+21 38 49.1	22.3	?
23	12 22 22.21	+21 39 43.7	23.1	g

1335−061

01[a]	13h35m31.s17	−06°11′57.″3	17.9	s
02	13 35 31.83	−06 12 03.0	19.5	s
03	13 35 30.16	−06 11 45.5	19.3	s
04	13 35 29.03	−06 12 08.2	20.8	g
05	13 35 29.59	−06 12 09.6	22.7	g
06	13 35 30.48	−06 12 18.9	22.5	g
07	13 35 30.33	−06 12 29.5	22.4	g
09	13 35 32.80	−06 12 11.2	22.2	g
10	13 35 32.59	−06 12 03.3	22.3	g
11	13 35 33.25	−06 12 03.8	21.4	g
12	13 35 33.17	−06 11 47.5	22.7	g
13	13 35 31.71	−06 11 48.7	22.0	g
14	13 35 31.05	−06 11 40.9	21.9	g
15	13 35 29.96	−06 11 34.0	21.8	g
16	13 35 31.25	−06 11 51.5	23.1	g
17	13 35 31.42	−06 11 52.9	22.4	g
19	13 35 30.53	−06 11 55.2	22.0	g
20	13 35 31.18	−06 12 04.3	23.5	?
28	13 35 29.00	−06 11 55.1	23.0	g
29	13 35 29.15	−06 11 49.3	23.8	g

1423+242

01[a]	14h23m34.s67	+24°17′32.″7	17.4	s
02	14 23 32.34	+24 17 22.8	19.1	s
03	14 23 32.84	+24 17 11.2	23.5	g
04	14 23 34.41	+24 17 03.2	21.5	g
06	14 23 36.53	+24 17 03.9	22.4	g
07	14 23 34.19	+24 17 29.4	23.5	g
09	14 23 35.47	+24 17 21.2	23.8	s
14	14 23 36.01	+24 17 30.2	23.6	g
15	14 23 35.57	+24 17 31.3	22.8	g
16	14 23 34.55	+24 17 38.8	23.3	?
17	14 23 35.01	+24 17 38.6	21.8	g
18	14 23 35.13	+24 17 38.8	21.7	g
20	14 23 36.37	+24 17 46.2	22.3	g
21	14 23 36.68	+24 17 52.0	22.2	g
22	14 23 36.41	+24 18 03.1	22.5	g
25	14 23 35.39	+24 17 58.4	23.4	s
29	14 23 33.51	+24 18 01.9	23.2	g
30	14 23 34.30	+24 17 57.1	21.3	s
31	14 23 35.23	+24 17 41.9	20.7	g

1512+370

01[a]	15h12m46.s90	+37°01′54.″0	16.0	s
02	15 12 47.73	+37 01 50.8	19.7	g
03	15 12 44.85	+37 01 55.7	20.6	g
04	15 12 45.19	+37 01 43.4	20.4	g
05	15 12 44.75	+37 01 42.8	20.7	g
06	15 12 44.67	+37 01 33.0	19.9	s
07	15 12 45.34	+37 01 26.2	20.8	g
08	15 12 47.01	+37 01 26.2	21.6	g
09	15 12 47.45	+37 01 23.6	21.2	g
10	15 12 48.11	+37 01 51.8	22.0	s
11	15 12 47.89	+37 01 57.2	22.3?	g
12	15 12 47.79	+37 02 09.8	22.2	g
13	15 12 49.12	+37 02 11.3	22.1	g
14	15 12 46.44	+37 01 57.0	21.3	g
17	15 12 46.49	+37 01 25.1	22.1	g
22	15 12 44.51	+37 02 16.9	22.9	s

1618+177

01[a]	16h18m07.s29	+17°43′30.″8	17.2	s
02	16 18 07.33	+17 43 23.5	21.4	g
03	16 18 08.13	+17 43 17.5	22.2	g
04	16 18 07.87	+17 42 57.8	22.6	g
06	16 18 07.05	+17 43 12.0	23.4	s
07	16 18 06.48	+17 43 10.7	22.5	g
08	16 18 06.39	+17 43 24.1	22.8	g
09	16 18 05.52	+17 43 03.6	21.2	s
10	16 18 05.94	+17 43 46.2	23.7	g
11	16 18 06.27	+17 43 43.9	22.7	g
12	16 18 06.40	+17 44 00.7	20.9	g
13	16 18 06.54	+17 43 52.3	23.3	s
15	16 18 07.03	+17 43 57.2	22.9	g
16	16 18 08.37	+17 43 52.6	23.6	g
17	16 18 08.46	+17 43 43.5	21.0	g
18	16 18 08.60	+17 43 35.8	22.4	g
19	16 18 07.17	+17 43 40.7	22.3	g
21	16 18 07.89	+17 43 33.2	23.5	s?

1741+279

01	17h41m57.s65	+27°54′22.″0	17.8	s
02[c]	17 41 57.97	+27 54 04.8	18.1	g
03	17 41 57.74	+27 54 02.1	18.6	s
04	17 41 59.17	+27 54 32.1	16.9	s
05	17 42 00.26	+27 54 17.1	17.3	s
06	17 41 56.91	+27 53 40.4	18.3	s
07	17 41 56.66	+27 54 30.2	18.8	s
08	17 41 56.38	+27 54 26.4	19.7	s
09	17 41 56.26	+27 54 08.0	20.3	s
10	17 41 55.53	+27 54 03.5	21.2	g, E
11	17 41 55.78	+27 53 50.0	20.0	s
12	17 41 55.58	+27 53 52.8	22.1	g
13	17 41 56.38	+27 53 49.7	22.9	g
14	17 41 57.28	+27 53 55.6	22.1	s
15	17 41 57.86	+27 53 55.3	22.7	g
16	17 41 58.35	+27 53 59.5	21.6	g
17	17 41 58.24	+27 53 48.6	22.1	g
18	17 41 58.87	+27 53 44.5	21.2	g
19	17 41 59.25	+27 53 48.6	23.2	g
20	17 41 59.46	+27 53 51.5	22.9	s
21	17 41 59.01	+27 53 55.3	22.4	g
22	17 41 59.85	+27 54 02.8	20.3	g
23	17 41 59.26	+27 54 06.2	21.7	g
24	17 41 59.18	+27 54 08.0	22.1	g
25	17 42 00.31	+27 53 32.7	21.8?	g

TABLE 2—*Continued*

Object	α(1950)	δ(1950)	R'_7	Class
		2353+283		
01[a]	$23^h53^m21^s.41$	+28°19′16″.3	17.6	s
02	23 53 21.59	+28 19 30.0	19.3	g
03	23 53 21.95	+28 19 08.2	21.2	g
04	23 53 23.21	+28 18 58.1	21.5	g
06	23 53 23.28	+28 19 11.9	22.0	s
07	23 53 23.05	+28 19 38.0	21.8	g
08	23 53 22.97	+28 19 34.6	22.8	g
09	23 53 21.94	+28 19 34.8	22.1	g
10	23 53 19.78	+28 19 38.0	22.1	g
12	23 53 20.21	+28 18 43.9	20.7	g
13	23 53 21.71	+28 19 03.4	23.1	g
14	23 53 22.42	+28 19 15.9	23.1	s

[a]QSO.
[b]QSO. FOCAS assigned 30% of flux in this object to a resolved component.
[c]QSO. FOCAS results indicate that ~25% of flux from this object is in a resolved component.

near the edge of the frame will be ~0″.5 due to scale errors and 0″.2 due to rotation. Because of the scale of the video camera data, the random measuring errors in relative positions of objects within a given video camera field are smaller than these expected systematic errors.

The positions, magnitudes, and classifications ("galaxy" or "star") derived for objects detected in each of the video camera fields are listed in Table 2. Finding charts for these objects are provided in Figure 1. Photographic reproductions of frames containing QSOs with evident underlying nebulosities are provided in Figures 2*a*–2*f* (Plates 4–9). These photographs were printed to emphasize the faintest galaxies detected. Because of the limited dynamic range of the DICOMED system used to produce the negatives, the brighter objects in each field, including all of the QSO cores, are saturated. Large magnitude differences between objects in a given field are often masked by this effect.

IV. SPECTROSCOPIC OBSERVATIONS

In order to confirm the apparent QSO–galaxy and QSO–cluster associations identified in our video camera observations, spectroscopy is being obtained for the galaxies detected. Initial results for three fields are reported here.

The spectra were obtained using the KPNO cryogenic camera on the 4 m telescope. The cryogenic camera is a low-dispersion, high quantum efficiency spectroscopic system utilizing a transmission grating and CCD detector (De Veny 1982). This system allows redshifts to be determined for absorption-line objects with R magnitudes exceeding 21.

In order to obtain simultaneous observations of several objects in each field, multiple 2″.5 holes were drilled in focal plane "aperture plates" using the positions listed in Table 2. Previous experience has demonstrated that focus and response variations in the cryogenic camera system preclude highly accurate sky subtraction if the "sky" and "object" spectra are obtained from different portions of the cryogenic camera fields. Therefore, "sky" holes were drilled immediately adjacent to each "galaxy" hole.

The grism used (KPNO 770) was ruled at 300 lines mm^{-1}, with a central wavelength of 6000 Å and an effective resolution of ~14 Å. The wavelength coverage obtained was limited by the CCD response, which is negligible below 4800 Å, and by atmospheric emission and absorption redward of ~8000 Å. The integration time for each field was between 6000 and 12000 s, but the integration times are poor indicators of the signal-to-noise obtained, since data quality is heavily dependent on seeing and transparency.

A quartz continuum lamp and a He-Ne-Ar source were observed through the aperture plate being used before and after each half-hour integration on the QSO field. During data reductions on the KPNO Cyber, the quartz calibrations were used to correct for pixel-to-pixel response variations in the CCD. Wavelength calibrations were determined for each spectrum using the He-Ne-Ar observations obtained through the same aperture. These calibrated data were then converted into a series of one-dimensional "object" and "sky" spectra. Using software developed by the KPNO staff for use on the Observatory's VAX computers, these spectra were wavelength-calibrated and sky-subtracted.

Spectroscopic data for those galaxies for which redshifts could be determined are provided in Table 3. The identifications are taken from Figure 1 and the magnitudes from Table 2, except for the 3C275.1 field, for which identifications and photometry were published by HBS.

V. DISCUSSION OF THE DIRECT OBSERVATIONS

An analysis of the direct data provides support at a high level of significance for both the cosmological interpretation of QSO redshifts and the hypothesis that wide-angle radio tail QSOs are members of clusters of galaxies. The primary results of the direct observations are summarized in Table 1 and Figure 4. The parameters used are defined in detail in the notes to Table 1. In determining the number of "excess" galaxies in each field, $\Delta N_{\rm lim}$, only galaxies brighter than the field completeness limit, R(comp), are included, and the counts are limited to the 1.17 square arc minute area processed by FOCAS. The background galaxy densities used are taken from the relation derived by Butcher and Oemler (1978), modified to include the 25% correction determined by Butcher, Oemler, and Wells (1983).

a) The Nature of QSO Redshifts

It is evident from Table 1 that substantial numbers of "excess" galaxies surround many of the lower redshift QSOs and that the number of excess galaxies observed drops precipitously at higher redshifts, as expected if QSO redshifts are cosmological. To allow a quantitative test of this result, we define ΔM to be the difference between the magnitude of the "completeness limit" and the predicted R magnitude of a first-ranked cluster galaxy at the QSO's redshift (Coleman, Wu, and Weedman 1980). The ΔM value for a field (Table 1) therefore provides an approximately redshift-independent indication of the sensitivity of our direct observations to a group or cluster of galaxies associated with the QSO, assuming the QSO's redshift is cosmological. If so, we would expect to detect few QSO-associated galaxies in fields with small ΔM, since our observations in those cases would not extend very

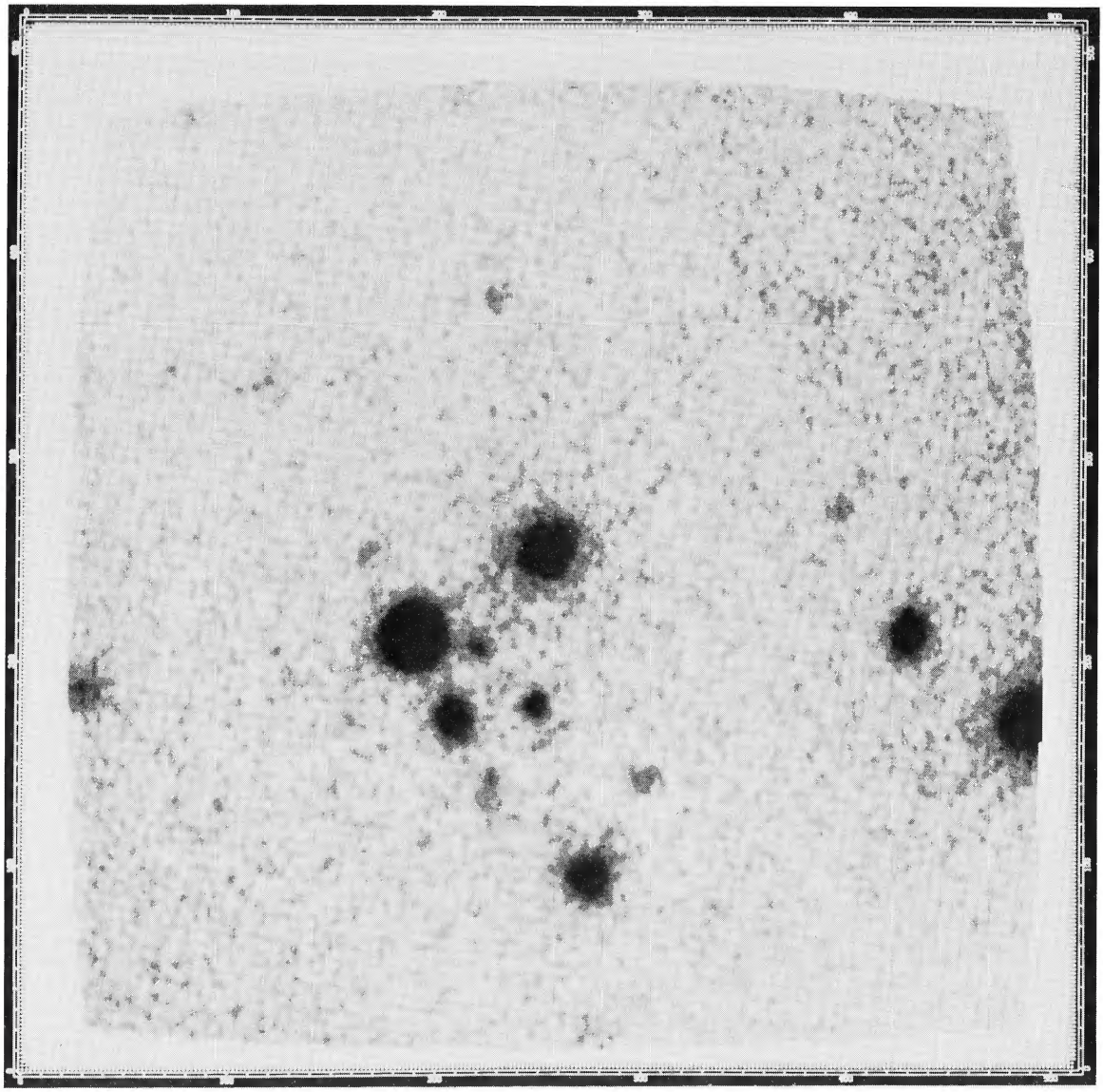

FIG. 2*a*

FIG. 2.—Direct data for QSOs with evident underlying nebulosities. (*a*) An *R* frame of 0903+169 (3C215, $z = 0.411$). North is at the top, east is to the left, and the field is $\sim 67''$ across and centered on the QSO. The QSO image includes both a point source and a resolved underlying component which contains between 30% and 45% of QSO flux. Field contains 6.5 excess galaxies with $R \leq 22.5$.

HINTZEN (*see* page 539)

PLATE 5

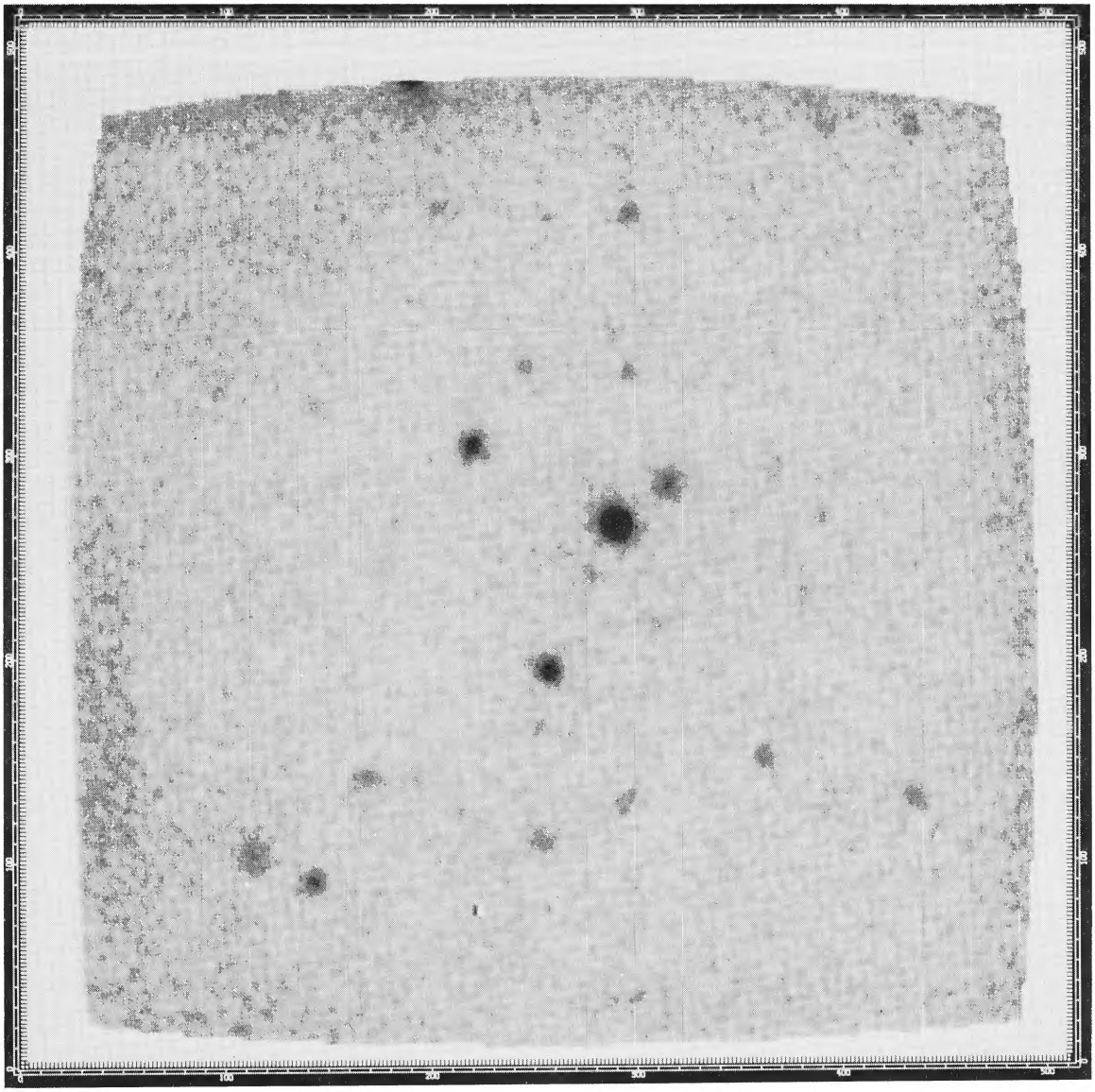

FIG. 2*b*

FIG. 2*b*.—Fourteen minute *V* frame of 1251+166 (3C275.1, $z = 0.555$). North is at top, east is to the left. This frame, taken on the KPNO 2.1 m telescope, is ~150″ across and centered slightly south of the QSO. The QSO image appears stellar, in contrast to its appearance in our deep *R* integration (Fig. 2*c*).

HINTZEN (*see* page 539)

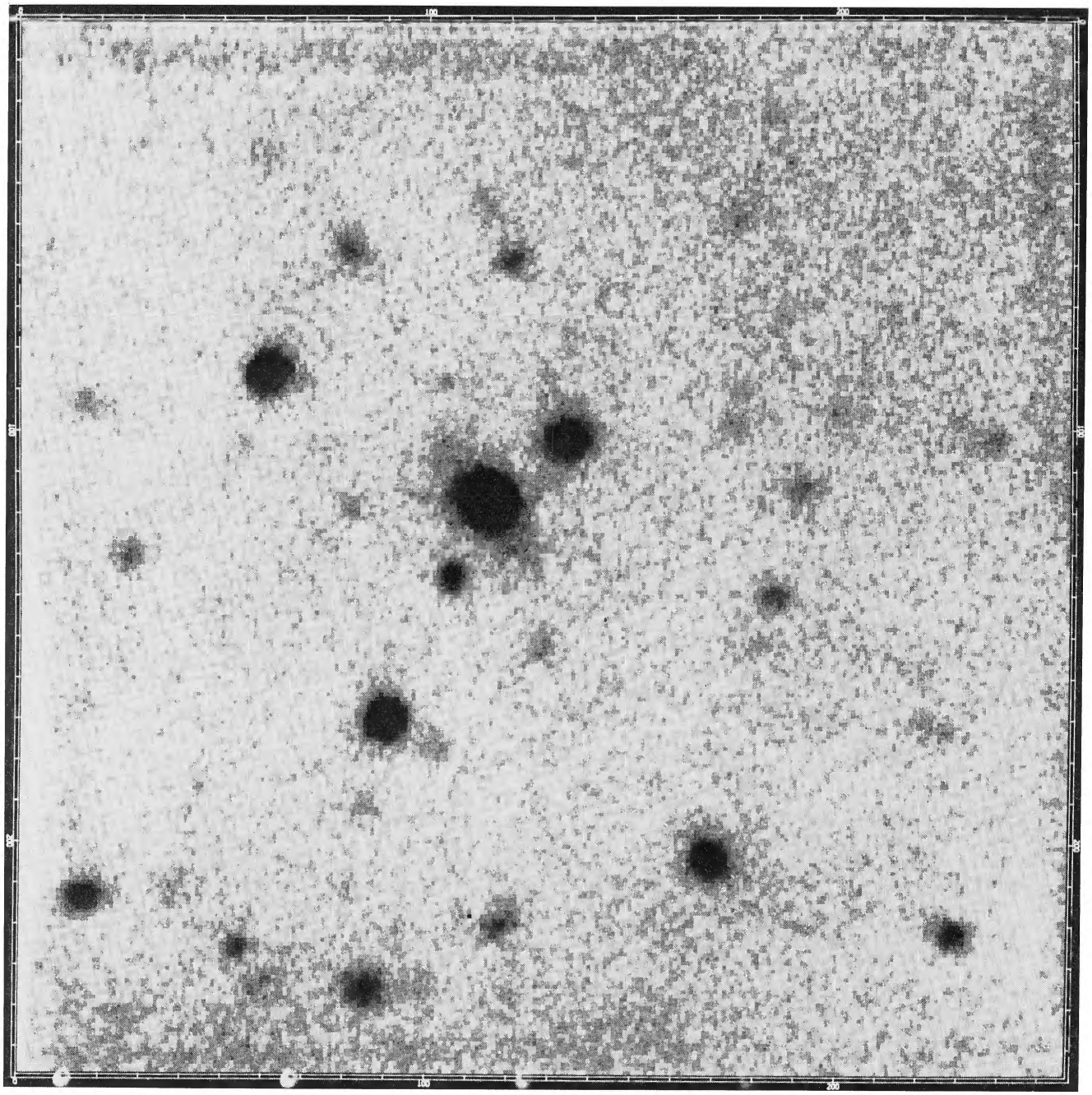

FIG. 2*c*

FIG. 2*c*.—Deep *R* frame of 1241+166 (3C275.1, $z = 0.555$). North is at top, east is to the left, and the frame is $\sim 67''$ across and centered on the QSO. Note the extremely large, faint nebulosity (14″ major axis) underlying the quasar (compare with the *V* frame in Fig. 2*b*). This field contains 22 excess galaxies brighter than the completeness limit ($R = 23$), and our spectroscopy of galaxies in the field (§ IV) provides preliminary confirmation of the suggestion that 3C275.1 lies in a first-ranked galaxy at the center of a rich cluster of galaxies (Hintzen, Boeshaar, and Scott 1981).

HINTZEN (*see* page 539)

PLATE 7

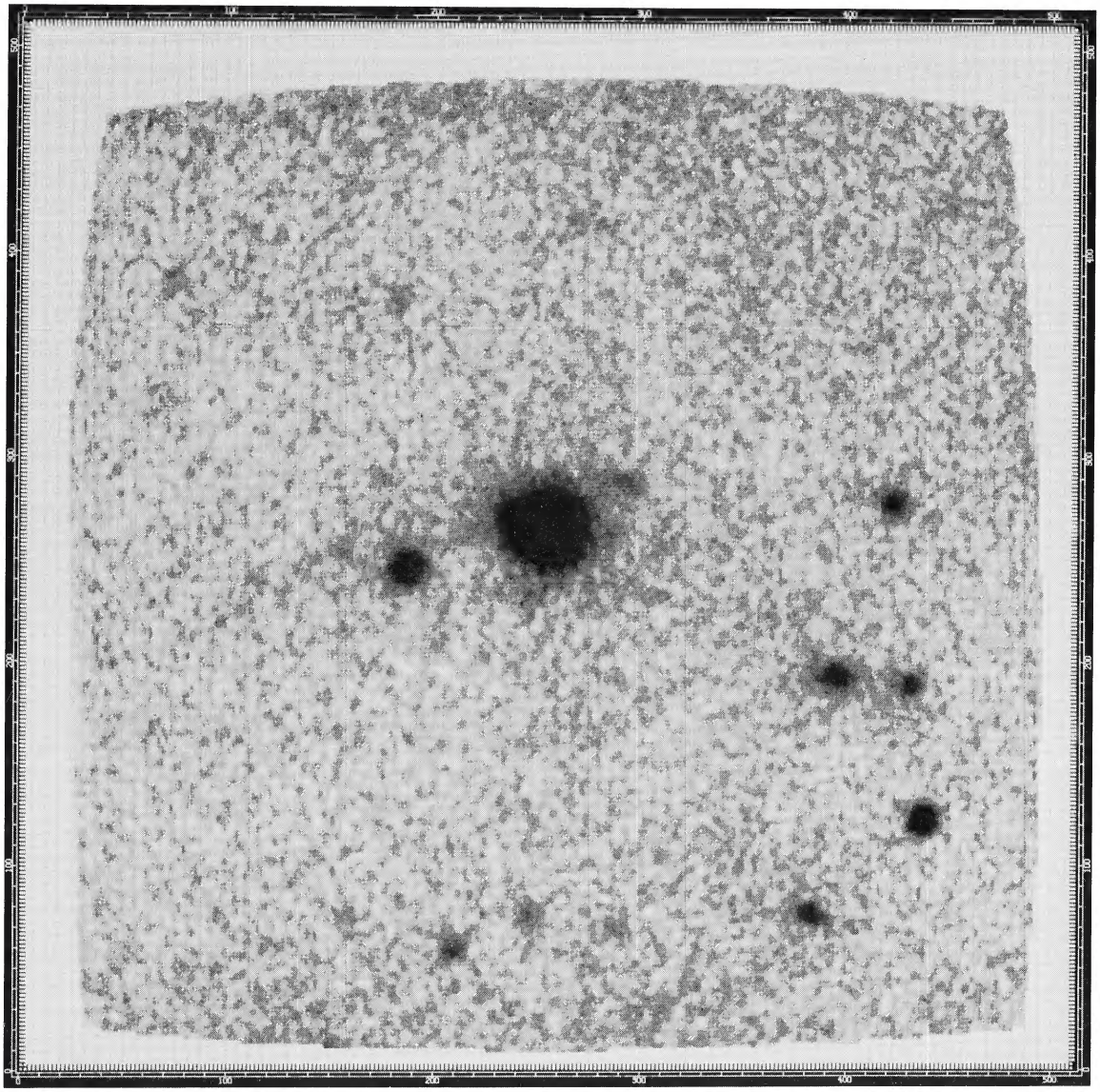

FIG. 2*d*

FIG. 2*d*.— *R* frame of 1512+370 (4C37.43, $z = 0.371$). North is at top, east is to the left, and the frame is ~ 67″ across and centered on the QSO. An irregular nebulosity underlies the QSO (see also Stockton 1976). This field contains eight excess galaxies with $R \leq 22.5$, and galaxy 2, 10″ east of the QSO, has essentially the same redshift as the QSO (Stockton 1978).

HINTZEN (*see* page 539)

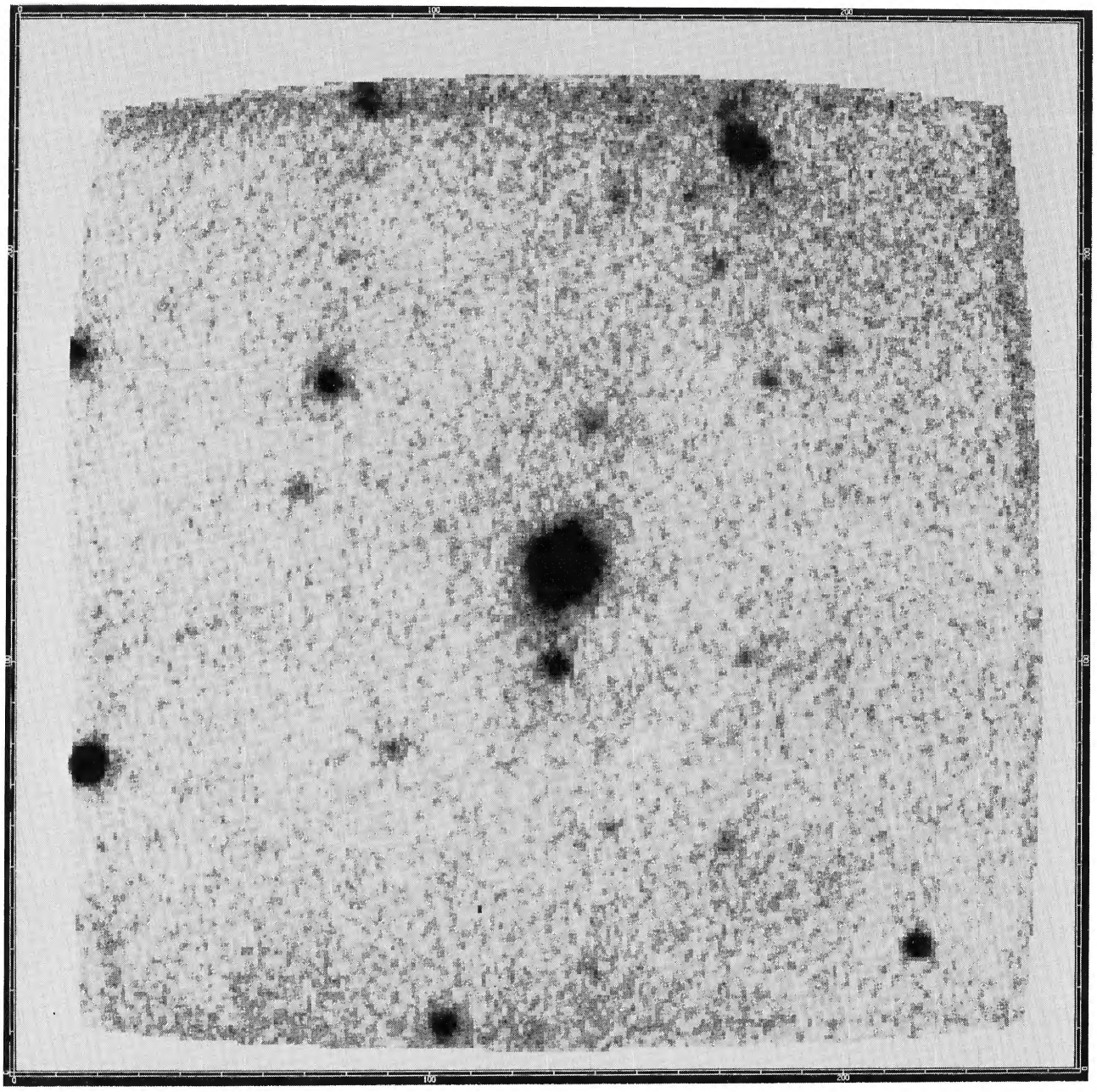

FIG. 2*e*

FIG. 2*e*.— *R* frame of 1618+177 (3C334, $z = 0.555$). North is at top, east is to the left, and the frame is $\sim 67''$ across and centered on the QSO. The QSO image is extended at a position angle of $\sim 160°$. This object and 3C275.1 (Fig. 2*c*) are the highest redshift QSOs in which resolved underlying components have been reported to date. Field contains 5.5 excess galaxies with $R \leq 23$.

HINTZEN (*see* page 539)

PLATE 9

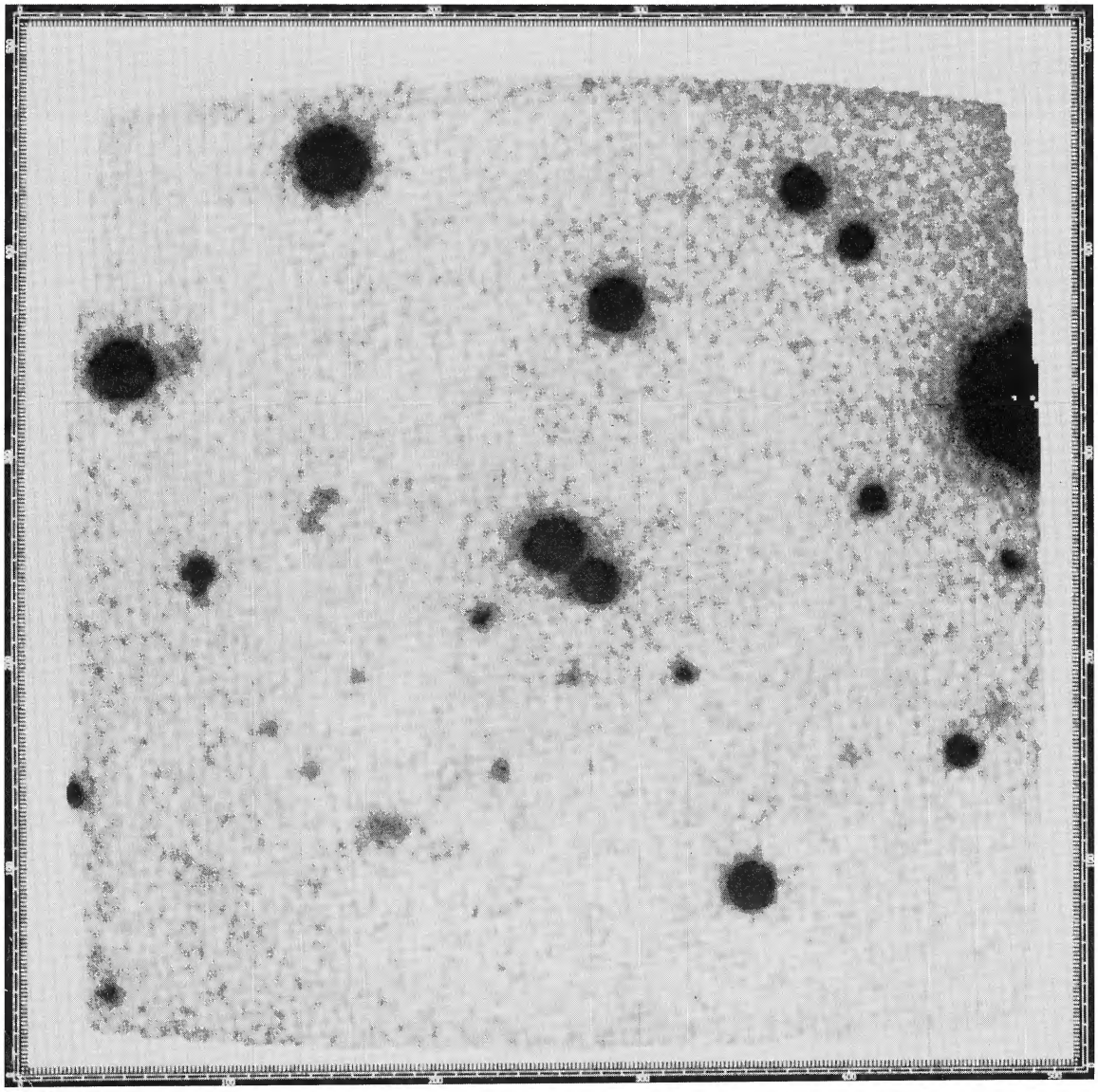

FIG. 2*f*

FIG. 2*f*.— *R* frame of 1741+279 (4C27.28, $z = 0.372$). North is at top, east is to the left, and the frame is $\sim 67''$ across and centered on the QSO. Between 25% and 50% of flux from the QSO is contained in a resolved, elliptically shaped component underlying the stellar nucleus. Field contains 5.5 excess galaxies with $R \leq 23$.

HINTZEN (*see* page 539)

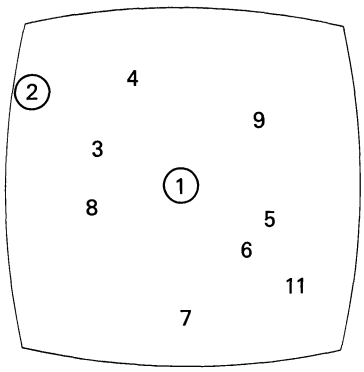

0003+158

FIG. 1*a*

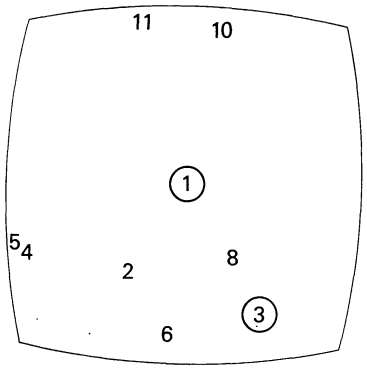

0115+027

FIG. 1*b*

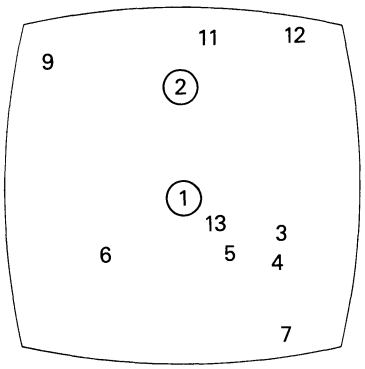

0118+034

FIG. 1*c*

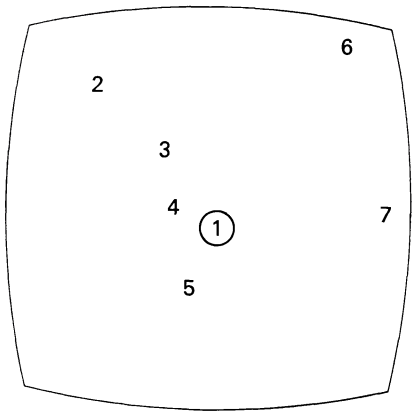

0130+242

FIG. 1*d*

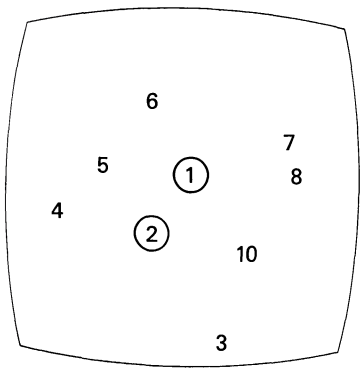

0214+108

FIG. 1*e*

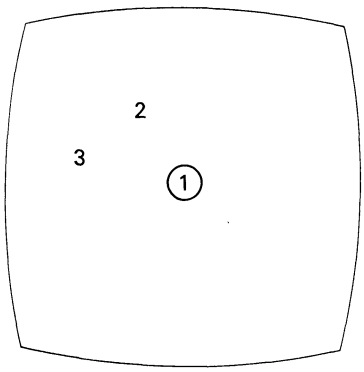

0340+048

FIG. 1*f*

FIG. 1.—(*a*)–(*q*) Finding charts for the objects detected in each field. North is up, east is to the left, and the fields are ~ 67″ across. Some objects identified are fainter than the completeness limit adopted in Table 1. Objects brighter than $R = 19$ are circled.

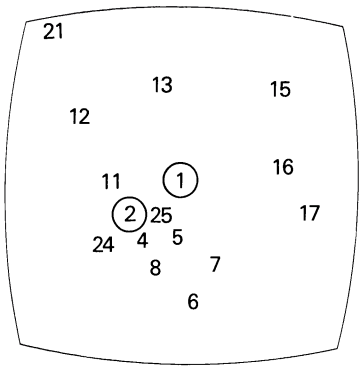

0903+169

FIG. 1*g*

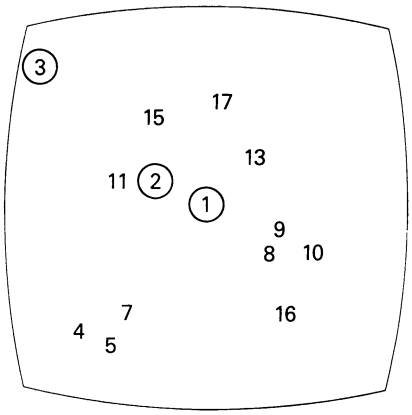

0957+003

FIG. 1*h*

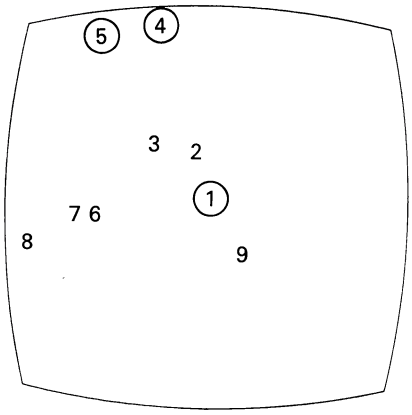

1038+52

FIG. 1*i*

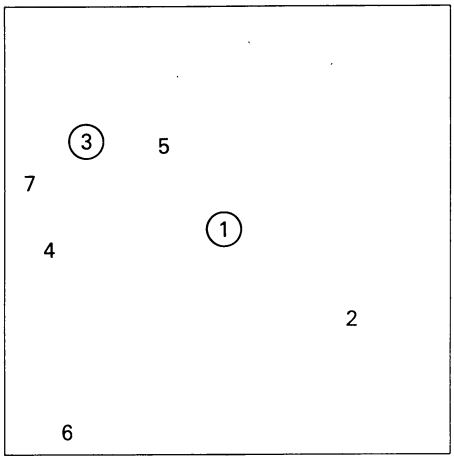

1100+772

FIG. 1*j*

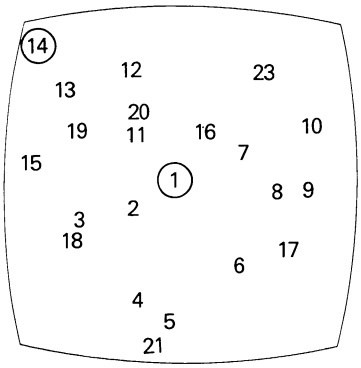

1222+216

FIG. 1*k*

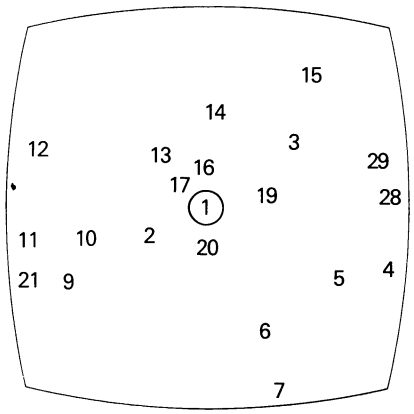

1335−061

FIG. 1*l*

FIG. 1.—*Continued*

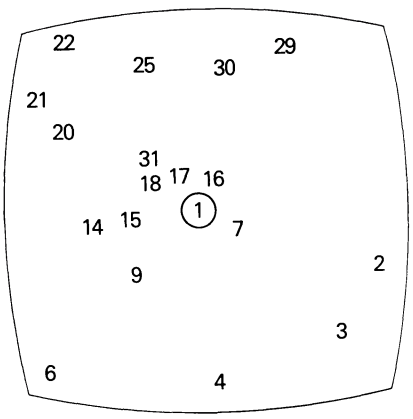

1423+240

FIG. 1*m*

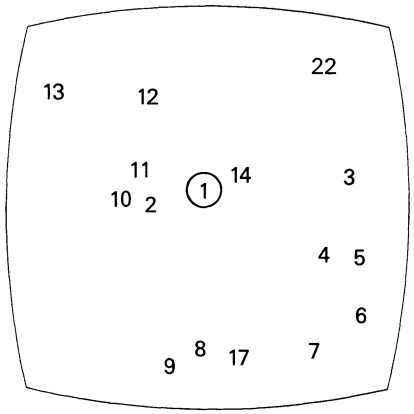

1512+37

FIG. 1*n*

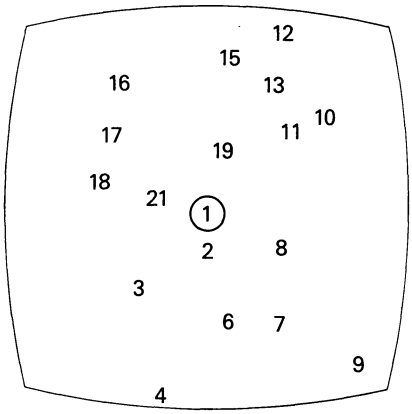

1618+177

FIG. 1*o*

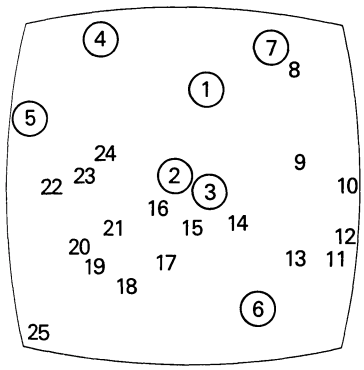

1741+279

FIG. 1*p*

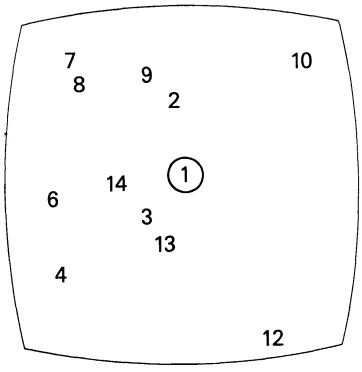

2353+283

FIG. 1*q*

FIG. 1.—*Continued*

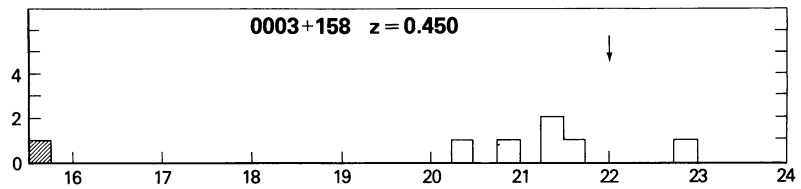

FIG. 3*a*

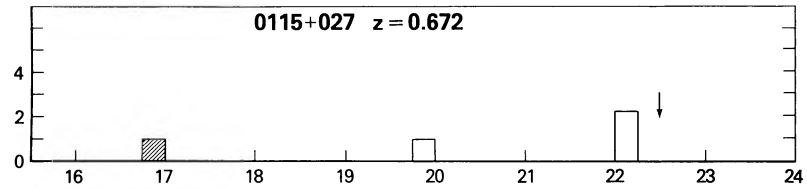

FIG. 3*b*

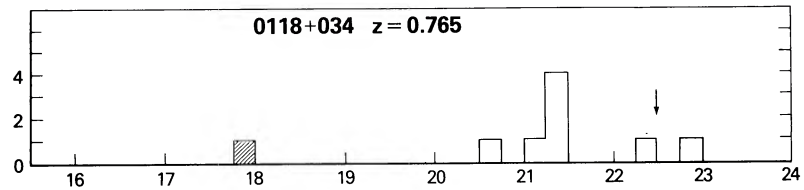

FIG. 3*c*

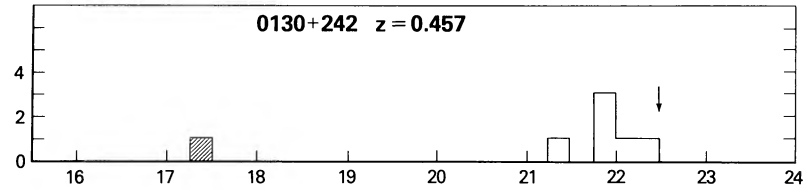

FIG. 3*d*

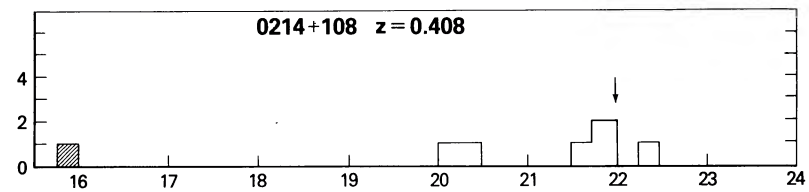

FIG. 3*e*

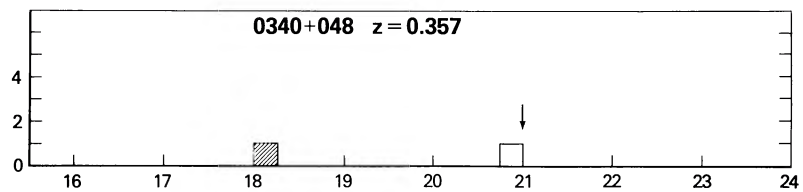

FIG. 3*f*

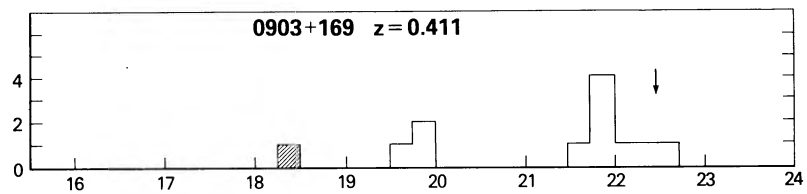

FIG. 3*g*

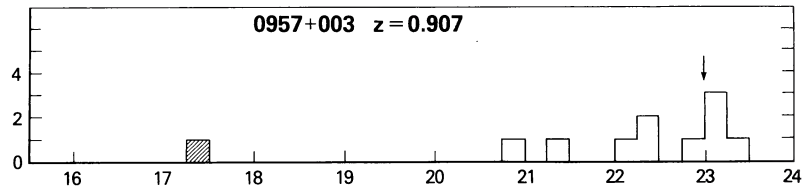

FIG. 3*h*

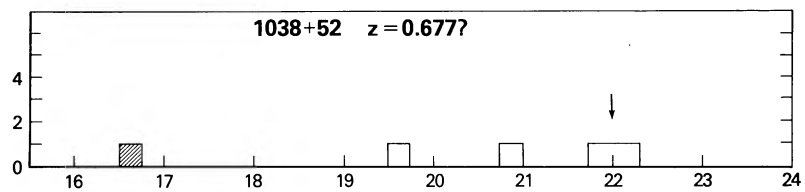

FIG. 3*i*

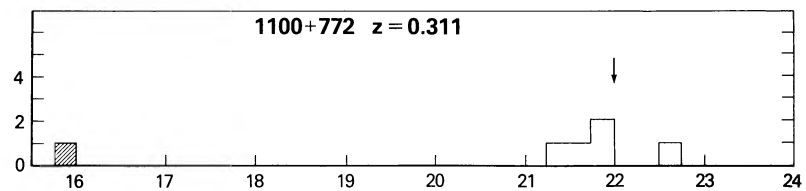

FIG. 3*j*

FIG. 3.—(*a*)–(*s*) Histograms for galaxies detected in each of the fields listed in Table 1. Photometry is from Table 2 or HBS. Only the QSOs, which are shaded, and objects within the FOCAS-reduced region which are classified as galaxies are plotted. Arrow indicates the magnitude adopted as the completeness limit.

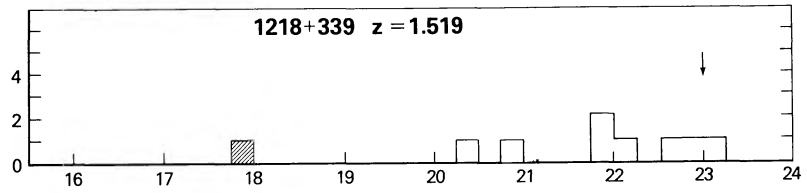

FIG. 3*k*

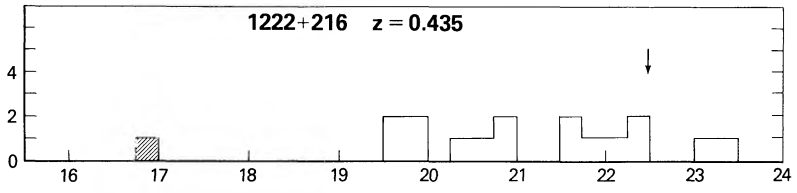

FIG. 3*l*

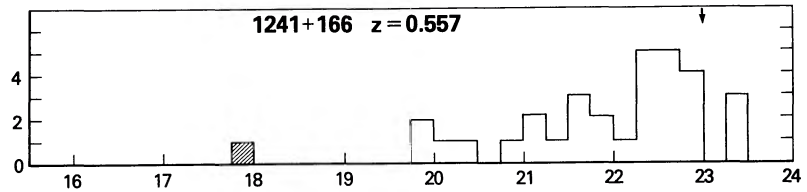

FIG. 3*m*

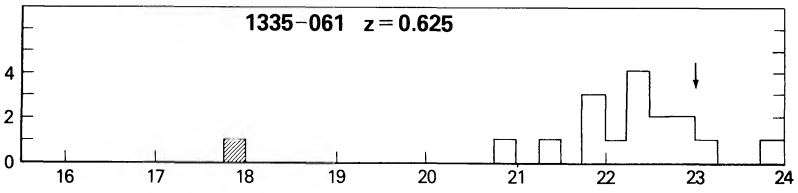

FIG. 3*n*

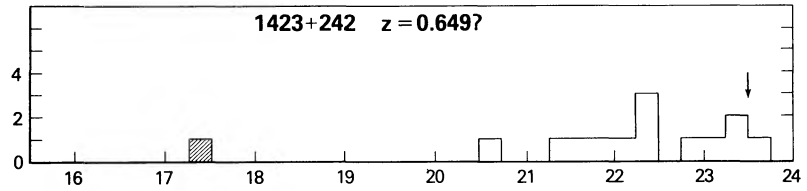

FIG. 3*o*

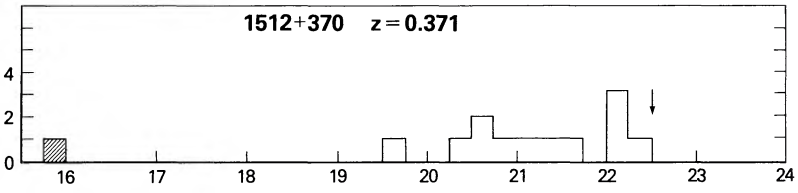

FIG. 3*p*

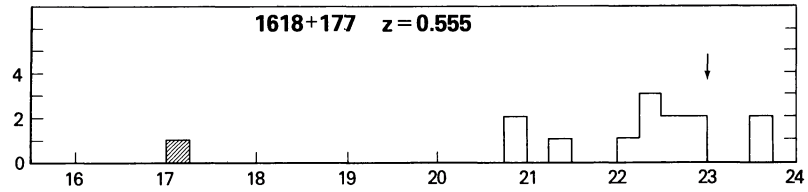

FIG. 3*q*

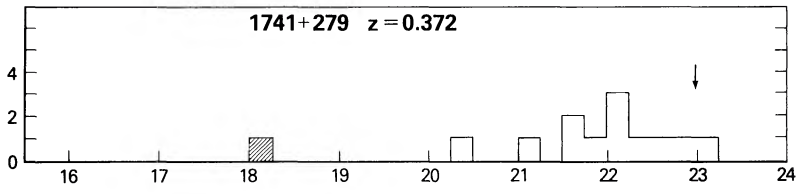

FIG. 3*r*

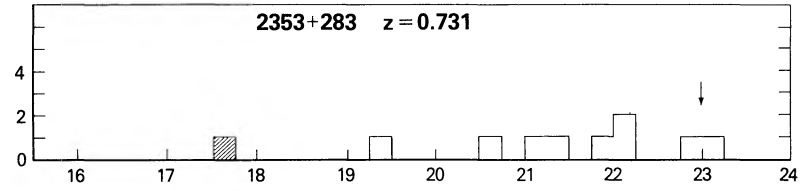

FIG. 3*s*

FIG. 3.—*Continued*

TABLE 3

SUMMARY OF SPECTROSCOPIC DATA

Object	m_R	Lines	z	$\bar{z}$ Error	Δv
0003+158-1 ..... (QSO)	15.4	Balmer, 3727 Å	...	0.4509 ±0.001	...
0003+158-5[a]	20.4	H K	0.3643 0.3654	0.3650? ±0.0005	−18.300.
0003+158-6	21.4	4000 Å H K 3727 Å	0.450 0.4515 0.4518 0.4500	0.4511 ±0.001	+41.
0003+158-7	21.6	5007 Å 4959 Å Hβ	0.2901 0.2900 0.2902	0.2901 ±0.0001	−35,100.
0214+108-1 ..... (QSO)	15.8			0.408	...
0214+108-3	20.2	G 4000 Å H K	0.4046 0.408 ... 0.4040	0.4055 ±0.0022	−530.
3C275.1-1 ..... (QSO)	18.0	Balmer, 3727 Å	...	0.5551 ±0.0003	...
3C275.1-2	21.2	4000 Å H K 3727 Å	0.553 0.5529 0.5543 0.5554	0.5539 ±0.001	−230.
3C275.1-4	19.8	5007 Å 4959 Å Hβ	0.1675 0.1670 0.1675	0.1673 ±0.0003	−83,700.
3C275.1-6	20.3	G 4000 Å H K	0.4649 0.465 0.4641 0.4662	0.4651 ±0.001	−17,900.
3C275.1-7[b]	21.6	3727 Å	0.5535	0.5535?	−307.

NOTES

Col. (1).—Object observed as identified in Fig. 1 or, in the case of 3C275.1, in HBS.

Col. (2).— R magnitudes are taken from Table 2 or HBS.

Cols. (3), (4).—Lines identified in the spectrum, with the corresponding redshift.

Col. (5).—Mean redshift derived for the object and the internal error estimate (rms dispersion of the z values for the individual lines).

Col. (6).—Relativistically correct velocity difference between the galaxy and QSO.

[a]The calcium lines seem well defined, but the 4000 Å break is not prominent, so the redshift is listed as uncertain.

[b]One strong emission line is present in each of the three integrations on galaxy 7. It is identified with O II λ3727 by elimination. The line is not O III λ5007, since O III λ4959 would be detectable. Similarly, identifying the line with Hβ appears unworkable, since O III λ5007 and Hγ are not detected at the appropriate redshifts. We therefore identify the line as O II λ3727.

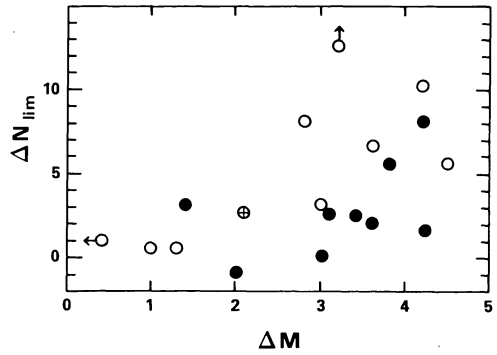

FIG. 4.—Number of excess galaxies in each QSO field is plotted as a function of ΔM, the difference between the R completeness limit of the field and the expected R magnitude of a first-rank cluster galaxy at the QSO's redshift. The ΔM values decrease with increasing redshift. Open circles denote wide-angle radio tail QSOs, the crossed circle indicates a possibly distorted QSO, and filled circles represent undistorted comparison QSOs. Objects with $\Delta M < 2.5$ constitute the high redshift sample ($z > 0.65$), and the fields of these QSOs contain an average of 1.1 ± 1.5 excess galaxies. The fields of QSOs in the low redshift sample ($\Delta M > 2.5$, $z \leq 0.65$) contain from 0 to 22 excess galaxies, with an average of 5.9. The large difference between the low redshift fields and the high redshift fields in the number of excess galaxies detected supports the cosmological interpretation of QSO redshifts at the 99% confidence level.

far down a typical cluster luminosity function. Of course, for fields with large ΔM (corresponding to small QSO redshifts, or large $R_{\rm lim}$, or both), groups or clusters of galaxies associated with the QSO should be detectable.[2]

These expectations are borne out by the data in Figure 4, in which $\Delta N_{\rm lim}$ is plotted as a function of ΔM for each of the QSO fields in the sample. Because of the absence of objects with $2.1 < \Delta M < 2.8$, the fields observed divide naturally into two subsamples. The first subsample ($\Delta M \leq 2.1$) includes all of the fields containing QSOs with $z > 0.65$ (hereafter called the high redshift fields). None of these six high redshift fields contains more than three excess galaxies, and the mean value is 1.1 ± 1.5 excess galaxies. By contrast, the 13 QSO fields with $\Delta M \geq 2.8$ (hereafter, the low redshift fields) each contains between 0 and 22 excess galaxies within approximately a 35″ radius of the QSO, with an average of 5.9 excess galaxies per field.

Note that for redshifts between 0.3 and 0.65, this 35″ radius corresponds to a linear distance of 0.2–0.3 Mpc ($H_0 = 50$ km s^{-1} Mpc^{-1}, $q_0 = 0$). This is approximately equal to the "core radius" of a rich cluster (Bahcall 1975), but far smaller than typical "limiting radii" of clusters (Bahcall 1977). Consequently, our observations would be expected to detect only a small fraction of the galaxies in a given QSO-associated cluster and would be relatively insensitive to clusters which are not approximately centered on the QSOs (see the examples cited in § I). On the other hand, restricting the galaxy counts to the immediate vicinity of the QSOs minimizes the possibility of contamination by foreground and background clusters and enhances the "detectability" of groups or clusters centered on the QSOs.

To assess the significance of the difference in galaxy counts between the low redshift and high redshift fields we employ the Wilcoxon (Mann-Whitney) rank-sum test (e.g., Alder and Roessler 1964; Harter and Owen 1973). The null hypothesis to be tested is that QSO redshifts are noncosmological, and, therefore, the general population of low redshift QSO fields does not, on average, contain a larger number of excess galaxies than does the general population of high redshift QSO fields. Using the Wilcoxon test to compare the $\Delta N_{\rm lim}$ values for the low and high redshift samples, the null hypothesis can be rejected at the 99% confidence level.

To ensure that this result is not affected by errors in the background counts, the analysis has been repeated on galaxy counts to a uniform magnitude limit ($R = 22.5$, Table 1). Only the 14 fields with $R(\text{comp}) \geq 22.5$ are included in this analysis, and background counts need not be subtracted, since the rank-sum test is independent of zero point. Assigning each field to the same subsample as before and applying the Wilcoxon test to the raw galaxy counts ($N_{22.5}$) for the high and low redshift subsamples, we again reject the null hypothesis, this time at the 98% confidence level. In view of the quantity of data deleted from the sample for this second test, the small drop in significance is not surprising. Our data therefore strongly support the cosmological interpretation of QSO redshifts (99% confidence).

b) RT QSOs as Members of Clusters of Galaxies

It is evident from Figure 4 that the statistical significance of the above result is primarily due to the presence in our sample of the RT QSO fields. Among the lower redshift objects ($\Delta M \geq 2.8$, $z < 0.65$), the six RT QSO fields contain an average of nine excess galaxies ($\Delta N_{\rm lim}$), while the seven comparison QSO fields contain on average three excess galaxies. If the Wilcoxon rank-sum test is used to compare the $\Delta N_{\rm lim}$ values for the low-redshift RT QSOs with those for the low-redshift comparison QSOs, the difference between these two subsamples is found to have a very large statistical significance.

However, if QSO redshifts are cosmological, the difference in $\Delta N_{\rm lim}$ values between the RT QSO fields and comparison QSO fields has been artificially enhanced by the dependence of "effective" field size on redshift. The mean redshift for RT QSOs in the low redshift sample ($z = 0.51$) is a bit larger than that for the comparison QSOs ($z = 0.42$). As a result, our observations tend to span a somewhat larger volume of space (at the QSO's distance) for the RT QSOs than for the comparison QSOs. To compensate for this effect, the excess galaxy counts have been converted to galaxy surface densities at the distances of the QSOs ($H_0 = 50$ km s^{-1} Mpc^{-1}, $q_0 = 0$). These excess galaxy surface densities ($\Delta N_{\rm lim}/A$) are repro-

[2]Since R(comp) was determined from photometry obtained through fixed apertures, the ΔM values listed are somewhat larger than would be obtained from "total" magnitudes, and the cluster "detectabilities" implied are overestimated. On the other hand, if galaxy evolution causes a significant change in galaxy absolute magnitude with increasing redshift, as numerical models imply (see Bruzual and Kron 1980), the R(1st) magnitudes used in calculating ΔM provide a somewhat pessimistic indicator of cluster detectability. Such considerations render the zero point for our ΔM scale somewhat arbitrary but do not affect the present analysis, since the *relative* ΔM values for the fields observed are being used to determine a logical redshift at which to divide the fields into "low redshift" and "high redshift" subsamples. For instance, if one applies Bruzual and Kron's evolutionary corrections for elliptical galaxies to the R(1st) and ΔM values in Table 1, the fields included in the high and low redshift subsamples remain the same.

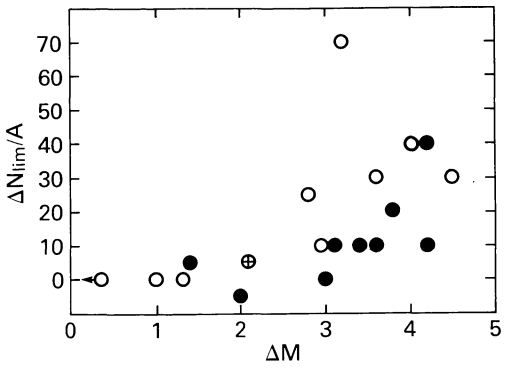

FIG. 5.—Abscissa for each point, ΔM, is the difference between the R completeness limit for that QSO field and the expected R magnitude of a first-ranked cluster galaxy at the QSO's redshift. Therefore, ΔM decreases with increasing redshift. The fields of the high redshift QSOs ($z > 0.65$) have $\Delta M \leq 2.1$, while the fields of the low redshift QSOs have $\Delta M \geq 2.8$. Ordinate for each field ($\Delta N_{\rm lim}/A$, Table 1) is the surface density of excess galaxies, in galaxies Mpc^{-2}, where the surface area A has been calculated at the distance corresponding to the QSO's redshift ($H_0 = 50$ km s^{-1} Mpc^{-1}, $q_0 = 0$). Open circles indicate RT QSO fields, crossed circle indicates a QSO which may be distorted, and filled circles correspond to the fields of undistorted QSOs. Restricting the discussion to the low redshift QSO fields ($z \leq 0.65$, $\Delta M \geq 2.8$), the Wilcoxon rank-sum test was used to compare the excess galaxy densities for the RT QSO fields with those for the comparison QSO fields. From this test we conclude with 97% confidence that RT QSOs are associated with greater concentrations of galaxies than are undistorted QSOs.

duced in Table 1 and plotted in Figure 5. Applying the Wilcoxon test to the $\Delta N_{\rm lim}/A$ values for the low-redshift fields in the RT QSO and comparison QSO subsamples, we can still reject at the 3% probability level the null hypothesis that the RT QSO fields do *not* systematically contain more excess galaxies than do the comparison QSO fields. Since the subsamples used in this test are comparatively small, the effect of changing these subsamples is worth noting. If either the 3C275.1 field ($\Delta N_{\rm lim}/A = 70$) or the 0340+048 field ($\Delta N_{\rm lim}/A = 0$) is deleted from the statistical test, the probability of reproducing from a single parent sample the $\Delta N_{\rm lim}/A$ values for both the RT QSOs and the comparison QSOs rises to 4.5% or 6.6%, respectively.

We conclude (97% confidence) that RT QSOs are associated with greater concentrations of galaxies than are undistorted QSOs. The distortions in the radio structures of the RT QSOs may therefore have been produced by interaction with intracluster media (ICM). W. Christiansen (private communication) has suggested that such distortions could also be produced when an ejected radio lobe ricochets off a galaxy near the QSO. This distortions mechanism would require the presence of neither an ICM nor a populous QSO-associated cluster. However, since the probability of producing a distorted source by this method would increase with the number of galaxies surrounding the radio QSO, we would still expect RT QSOs to preferentially occur in clusters of galaxies.

As noted earlier, the 65″ square fields analyzed by FOCAS would approximately subtend a typical cluster core (0.5 Mpc diameter) at the redshifts of the QSOs observed. Consequently, larger format direct observations are required to assess accurately the richness of the groups or clusters detected. Nevertheless, the cluster associated with the RT QSO 3C275.1 qualifies as rich based on the galaxies detected within the video camera frame alone (see § VI and HBS).

c) *Nebulosities Underlying the QSOs*

The comparatively large scale of the video camera data, 0.″292 per pixel, provides considerable sensitivity to extended structure underlying the QSOs. Detailed analysis of the QSO images is in progress, but it is evident from the data reproduced in Figure 2 that at least four of the QSOs observed ($z = 0.37$–0.55) display easily resolved components underlying the stellar nucleus. The two QSOs with $z = 0.55$ are the highest redshift quasars for which underlying nebulosities have been reported to date (Wyckoff, Wehinger, and Gehren 1981; Hutchings *et al.* 1982).

The nebulosity underlying 1241+166 (3C275.1, $z = 0.55$), although faint, is remarkably large, with a major axis of $\sim 14''$ (see HBS). It therefore has the largest linear dimensions of any underlying nebulosity discovered to date and lies well above the redshift–angular size relation derived by Wyckoff *et al.* for host galaxies of radio-loud QSOs. Two frames of the 3C275.1 field are reproduced in Figure 2. In the comparatively shallow V frame only the stellar nucleus of the QSO can be seen, surrounded by a few of the brighter galaxies in the field. The nebulosity underlying the QSO is evident in the deeper R frame, although the QSO nucleus and brighter galaxies are saturated in this print. The size of this nebulosity and the QSO's apparent position near the center of a rich cluster of galaxies suggest that 3C275.1 may lie in a cD galaxy or at least an object of cD-like dimensions.

The QSO 1618+177 (3C334) has a similarly large redshift ($z = 0.555$) and a decidedly elongated underlying nebulosity. The compact, high surface brightness galaxy lying 6″ south of the QSO resembles the compact galaxy associated with 1512+370 (Fig. 2 and Stockton 1978).

The other two easily resolved QSOs, 0903+169 (3C215) and 1741+279 (4C27.38), have considerably smaller redshifts ($z = 0.411$ and $z = 0.372$, respectively). The FOCAS analysis of the flux in 15 pixel rasters centered on the QSOs assigned 30% of the flux in the 0903+169 image and 25% of the flux in 1741+279 to resolved components twice the width of the stellar cores.

In addition, faint objects and irregular patches of nebulosity lie near or around several of the QSOs observed, producing irregularities in the QSOs' isophotes at low light levels. This effect is most clearly seen in 1512+370 (Fig. 2).

VI. DISCUSSION OF THE SPECTROSCOPIC OBSERVATIONS

While spectroscopic observations of the galaxies detected in the direct observations discussed above are still in progress, results are available for first-round integrations on three fields containing excess galaxies: 0003+158, 0214+108, and 3C275.1 (1241+166). Redshifts have been determined for eight galaxies detected in our video camera observations of these fields. The reduced spectra for these galaxies are reproduced in Figure 6, and the spectroscopic data are summarized in Table 3. The redshift listed in Table 3 for QSO 0214+108 was taken from Hewitt and Burbidge (1980), while those for 0003+158 and

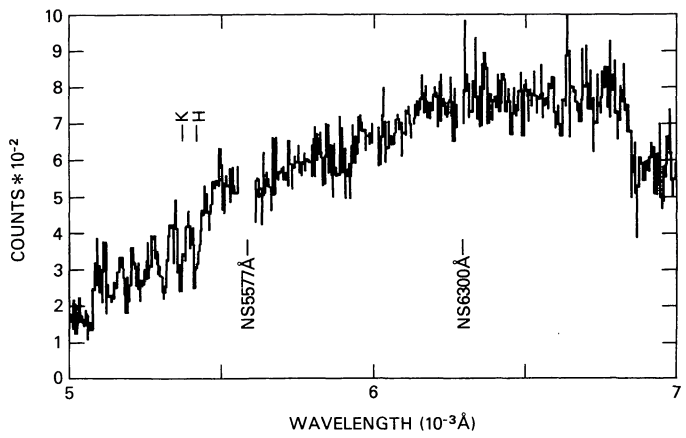

FIG. 6*a*

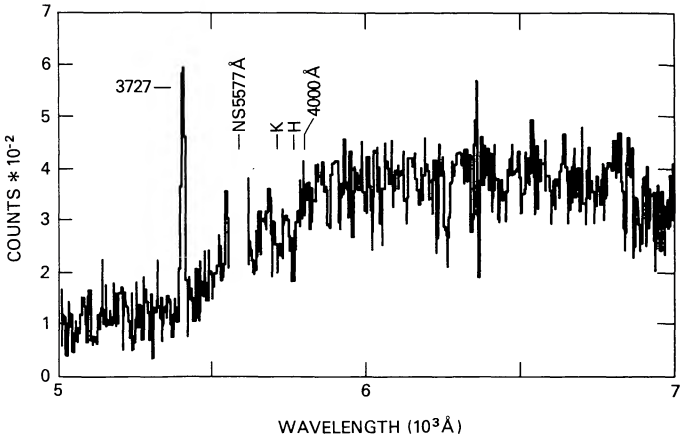

FIG. 6*b*

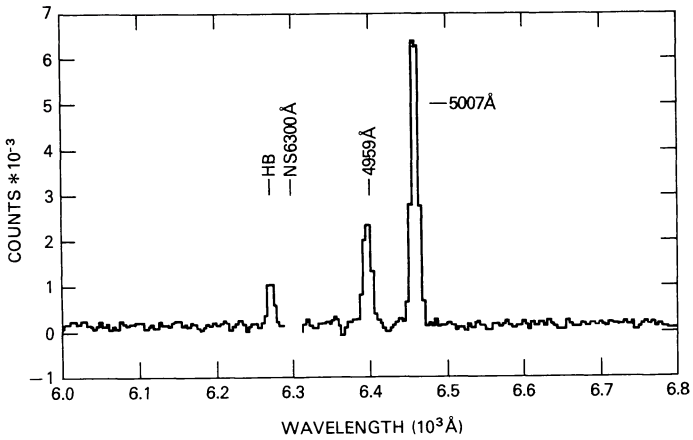

FIG. 6*c*

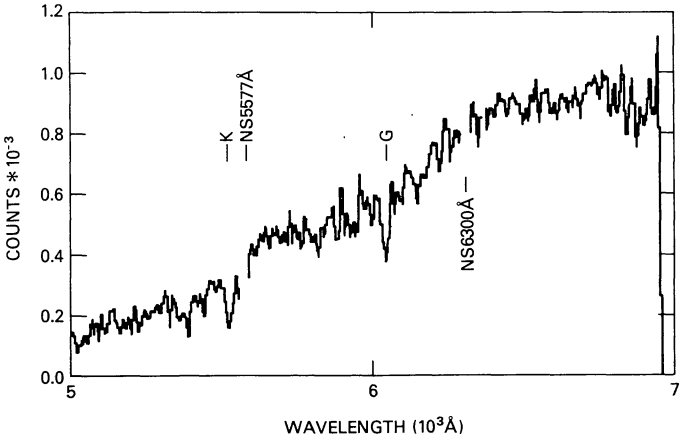

FIG. 6*d*

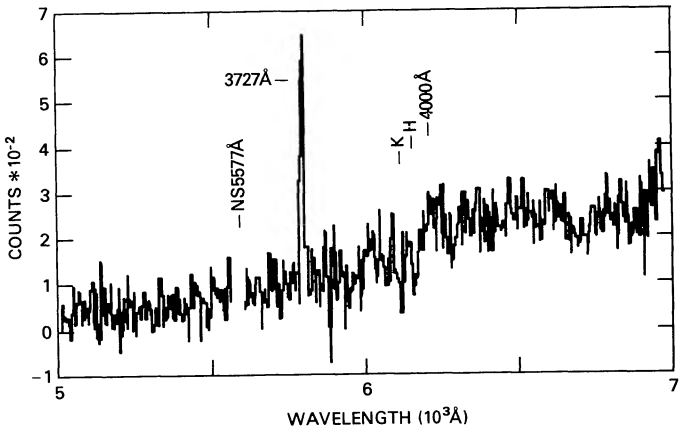

FIG. 6*e*

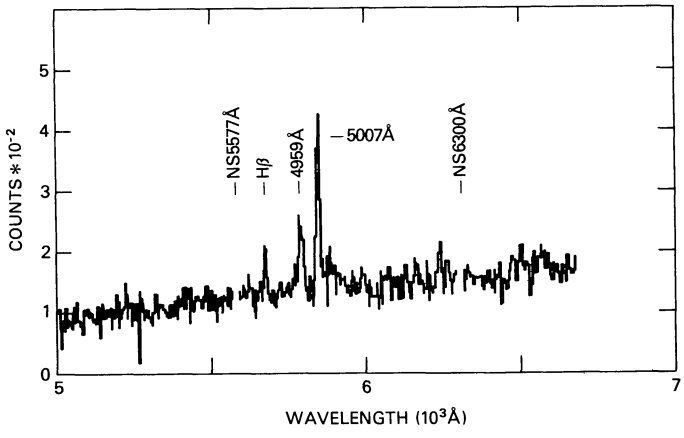

FIG. 6*f*

FIG. 6.—Reduced spectra for the galaxies listed in Table 3. Short gaps in the spectra are caused by deletion of the major night sky emission lines. (*a*) 0003+158-5; (*b*) 0003+158-6; (*c*) 0003+158-7; (*d*) 0214+108-3; (*e*) 3C275.1-2; (*f*) 3C275.1-4; (*g*) 3C275.1-6; (*h*) 3C275.1-7.

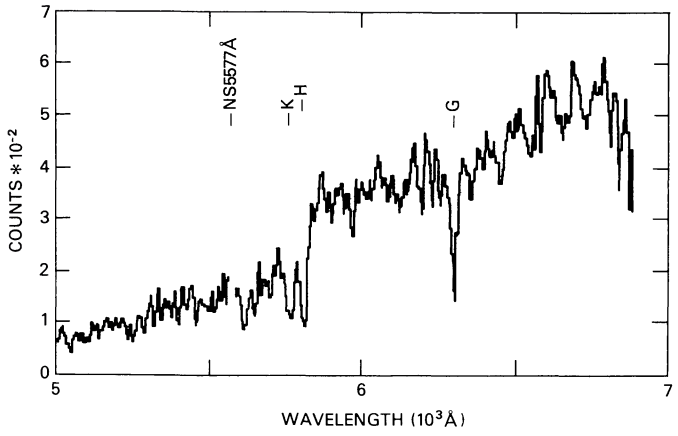

FIG. 6g

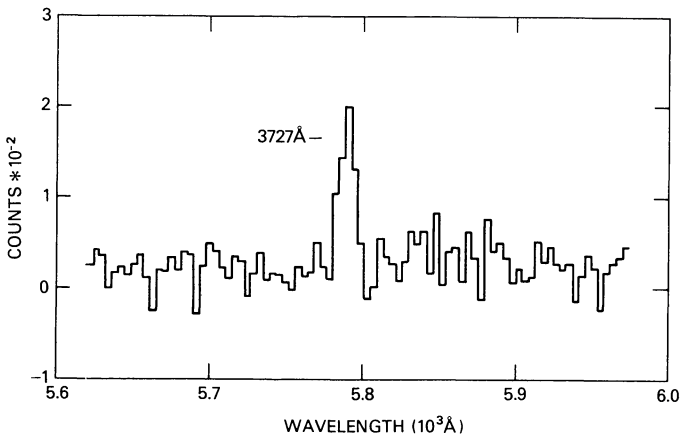

FIG. 6h

FIG. 6.—*Continued*

3C275.1 were derived from our cryogenic camera observations and agree well with the cataloged values.

As can be seen from the last column in Table 3, four of the eight galaxies listed have relativistically correct velocity differences with respect to the corresponding QSO of less than 600 km s^{-1}. The other four galaxies are all foreground objects; i.e., they have redshifts which are substantially smaller than those of the QSOs they appear to lie near. Also, Stockton (1978) reported that $v_{\rm galaxy}-v_{\rm QSO} = 300$ km s^{-1} for galaxy 2 in the 1512+370 (4C37.43) field. Therefore, spectroscopy is available for a total of nine galaxies in four of the QSO fields in our sample which contain excess galaxies, and at least one galaxy in each field has the same redshift as the corresponding QSO.

Since the spectra of three of the four QSO-associated galaxies listed in Table 3 contain strong [O II] λ3727, the referee has suggested that this emission might have been activated by ultraviolet radiation from the QSOs. On the other hand, most of the QSO-associated galaxies for which Stockton (1978) obtained spectra do not show strong O II emission.

The fact that half of the eight galaxies listed in Table 3 have essentially the same redshifts as the corresponding QSOs supports Stockton's (1978) conclusion that QSO redshifts are cosmological, since otherwise such a large percentage of QSO-galaxy redshift coincidences would be extremely improbable. The present data provide good S/N in the region of the 4000 Å break and O II λ3727 for redshifts between 0.25 and 0.625. We make the conservative assumption that all galaxies in our sample for which we can obtain redshifts have redshifts evenly distributed within this interval. Then the probability that three of seven galaxies will by chance have velocities within 1000 km s^{-1} of the corresponding QSOs is less than 0.001. (Galaxies 2 and 7 in the 3C275.1 field are counted as a single object, since they are associated with each other, as well as with the QSO). It is therefore very improbable that the QSO-galaxy redshift coincidences occurred by chance. These results provide confirmation that the excess galaxies detected in the QSO fields observed are indeed associated with the quasars.

The 3C275.1 field is of particular interest, since our video camera frame for this RT QSO contains about two dozen excess galaxies within 35″ of the QSO. As noted by HBS, four galaxies in the field have R magnitudes brighter than 20.3 and are likely to be foreground objects, in which case the underlying cluster would qualify as "rich" if it is at the distance indicated by the QSO's redshift. Our observations of two of the four bright galaxies confirm that they are indeed foreground objects ($z = 0.167$ and $z = 0.465$). The fact that the two fainter galaxies observed in the 3C275.1 field have the same redshift as the QSO strongly supports the suggestion of HBS that 3C275.1 lies near the center of a rich cluster. Further observations are therefore needed, since confirmation that QSOs can occur at the center of rich clusters of galaxies would have important implications for our understanding of the QSO phenomenon (see Stocke and Perrenod 1981).

VII. CONCLUSIONS

Deep direct observations have been obtained for the fields of 19 QSOs with redshifts between 0.3 and 1.5. Counts of "excess" galaxies in 1.17 square arc minute fields centered on the QSOs confirm the cosmological interpretation of QSO redshifts at the 99% confidence level and indicate with 97% confidence that wide-angle radio tail QSOs lie in richer concentrations of galaxies than do undistorted QSOs. Among the QSOs for which underlying nebulosities have been detected are 3C275.1 and 3C334. Both have redshifts of 0.55, making them the highest redshift QSOs for which resolved components have been identified.

Redshifts have been obtained for eight galaxies in three of the QSO fields containing "excess" galaxies, and Stockton (1978) has determined the redshift of the brightest galaxy in a fourth field. Five of these nine galaxies (at least one in each field) have essentially the same redshift as the corresponding QSO. This result provides confirmation that the "excess" galaxies detected in the QSO fields have the same redshifts as the QSOs.

Four of the galaxies for which redshifts have been obtained lie in the 3C275.1 field, which contains 22 excess galaxies brighter than $R = 23$ within $\sim 35''$ of the QSO. The two brighter galaxies observed ($z = 0.17$ and $z = 0.46$) are foreground objects, as expected (HBS). The two fainter galaxies have the same redshift as the QSO ($z = 0.55$), providing preliminary confirmation that this RT QSO lies at the center of a rich cluster of galaxies, the first such case identified.

The observations reported here indicate that deep CCD observations of the fields of RT QSOs would provide a sample of distant clusters of galaxies ($0.3 < z < 2$). at known redshifts (the QSOs'). Such a sample could be used to study the evolution of clusters and their constituent galaxies over very long time baselines and might allow an accurate determination of q_0 (e.g., Bruzual and Spinrad 1978). Observing RT QSOs rather than a general sample of high redshift QSOs should ensure the presence of a QSO-associated cluster in each field, minimizing the formidable problem of contamination of the sample by foreground and background clusters.

Thanks are due to the staff of KPNO and especially to Jeannette Barnes and Francisco Valdes for extensive assistance in the data analysis. We thank Wayne Christiansen and Hyron Spinrad for suggestions incorporated into the manuscript.

REFERENCES

Alder, H., and Roessler, E. 1964, *Introduction to Probability and Statistics* (San Francisco: Freeman).
Bahcall, N. 1975, *Ap. J.*, **198**, 249.
_____. 1977, *Ann. Rev. Astr. Ap.*, **15**, 505.
Baldwin, J., *et al.* 1977, *Ap. J.*, **215**, 408.
Bruzual, G., and Kron, R. 1980, *Ap. J.*, **241**, 25.
Bruzual, G., and Spinrad, H. 1978, *Ap. J.*, **220**, 1.
Burns, J., and Gregory, S. 1982, *A.J.*, **87**, 1245.
Butcher, H., and Oemler, A., Jr. 1978, *Ap. J.*, **219**, 18.
Butcher, H., Oemler, A., Jr., and Wells, D. 1983, *Ap. J. Suppl.*, **52**, 183.
Christian, C. 1980, Video Camera/CCD Standard Fields Manual (Tucson: KPNO).
Coleman, G., Wu, C., and Weedman, D. 1980, *Ap. J. Suppl.*, **43**, 393.
De Veny, J. 1982, An Observer's Manual for the Cryogenic Camera (Tucson: KPNO).
French, H., and Gunn, J. 1983, *Ap. J.*, **269**, 29.
Harter, H., and Owen, D. 1973, *Selected Tables in Mathematical Statistics* (Providence: American Mathematical Society).
Harris, D. E., Dewdney, P. E., Costain, C. H., Butcher, H., and Willis, A. G. 1983, *Ap. J.*, **270**, 39.
Hayes, D. 1982, *KPNO Newsl.*, No. 21.
Heiles, C. 1976, *Ap. J.*, **204**, 379.
Hewitt, A., and Burbidge, G. 1980, *Ap. J. Suppl.*, **43**, 57 (HB).
Hintzen, P., Boeshaar, G., and Scott, J. 1981, *Ap. J.* (*Letters*), **246**, L1 (HBS).
Hintzen, P., and Owen, F. 1981, *A.J.*, **86**, 1577.
Hintzen, P., Ulvestad, J., and Owen, F. 1983, *A.J.*, **88**, 709 (HUO).
Hutchings, J. B., Crampton, D., Campbell, B., Gower, A. C., and Morris, S. C. 1982, *Ap. J.*, **262**, 48.
Koo, D. 1981, *Ap. J.* (*Letters*), **251**, L75.
Margon, B., Downes, R., and Spinrad, H. 1983, *Nature*, **301**, 221.
Mould, J., Christian, C., Adams, M., and Stryker, L. 1980, User's Guide to the Kitt Peak Stellar Photometry Software (Tucson: KPNO).
Oemler, A., Jr., Gunn, J. E., and Oke, J. B. 1972, *Ap. J.* (*Letters*), **176**, L47.
Owen, F., and Rudnick, L. 1976, *Ap. J.* (*Letters*), **205**, L1.
Phillips, M. 1980, *Ap. J.* (*Letters*), **236**, L45.
Roberts, D., O'Dell, S., and Burbidge, G. 1977, *Ap. J.*, **216**, 227.
Rudnick, L., and Owen, F. 1977, *A.J.*, **82**, 1.
Sandage, A. 1973, *Ap. J.*, **183**, 711.
Spinrad, H. 1980, *IAU Symposium 92, Objects of High Redshift*, ed. G. O. Abell and P. J. E. Peebles (Dordrecht: Reidel), p. 30.
Stocke, J., and Perrenod, S. 1981, *Ap. J.*, **245**, 375.
Stockton, A. 1976, *Ap. J.* (*Letters*), **205**, L113.
_____. 1978, *Ap. J.*, **223**, 747.
Stockton, A. 1980, in *IAU Symposium 92, Objects of High Redshift*, ed. G. O. Abell and P. J. E. Peebles (Dordrecht: Reidel), p. 89.
Valdes, F. 1982, FOCAS User's Manual (Tucson: KPNO).
Wyckoff, S., Wehinger, P. A., and Gehren, T. 1981, *Ap. J.*, **247**, 750.
Wyckoff, S., Wehinger, P. A., Spinrad, H., and Boksenberg, A. 1980, *Ap. J.*, **240**, 25.

PAUL HINTZEN: Code 681, NASA Goddard Space Flight Center, Greenbelt, MD 20771